Geoscience Frontiers xxx (xxxx) xxx

HOSTED BY

ELSEVIER

Contents lists available at ScienceDirect

Geoscience Frontiers

journal homepage: www.elsevier.com/locate/gsf


Research Paper

# Rhyacian and Neoproterozoic magmatic associations of the Gurupi Belt, Brazil: Implications for the tectonic evolution, and regional correlations

Evandro L. Klein [a,b,*], Elem C.S. Lopes [c], Joseneusa B. Rodrigues [a], Sulsiene M. Souza-Gaia [c], Umberto G. Cordani [d]

[a] Geological Survey of Brazil - SBN, Quadra 02, Bloco H, Ed. Central Brasília, 1° Andar, Asa Norte, Brasília, DF, CEP: 70040-904, Brazil
[b] GPGE – Grupo de Pesquisa Em Geologia Econômica, PPGG – Programa de Pós-Graduação Em Geologia e Geoquímica, Universidade Federal Do Pará, Belém, PA, Brazil
[c] Geological Survey of Brazil, Av. Dr. Freitas, 3645, Belém, PA, CEP: 66095-110, Brazil
[d] Universidade de São Paulo, Instituto de Geociências, Rua Do Lago, 562, Cidade Universitária, São Paulo-SP, CEP: 05508-080, Brazil

ARTICLE INFO

Handling Editor: Nick M W Roberts

*Keywords:*
Neoproterozoic
Paleoproterozoic
Accretionary orogeny
Intracontinental orogeny
West Gondwana
Isotope geology

ABSTRACT

The Gurupi Belt, in north-northeastern Brazil, is a mobile belt developed in the south-southwestern margin of the São Luís cratonic fragment and crops out as a tectonic and erosional window within the Phanerozoic cover. Field, petrographic, geochemical, geochronological, and Nd isotopic information (new and published) constrain the timing and types of magmatic associations present in the belt and the tectonic settings in which they formed. The Rhyacian was the main period of magmatic activity, which can be grouped into two main stages. (1) ~2185–2130 Ma: pre-collisional, juvenile, calc-alkaline magnesian and calcic ferroan granitoid suites, and minor calc-alkaline and tholeiitic mafic plutonism (now amphibolites), formed in intra-oceanic to transitional/continental arcs; and intra- or back-arc volcano-sedimentary basin. (2) ~2125–2070 Ma: syn- (two-mica granites) to late-collisional (potassic to shoshonitic granites and quartz-syenite) plutonic suites produced after crustal thickening and melting, with localized migmatization, that intruded during the compressive $D_1$ deformational phase and concomitantly with greenschist to amphibolite metamorphism. There is a zonation of the Rhyacian episodes, with intra-oceanic stages occurring to the northeast, and the continental arc and collisional phases occurring to the southwest, indicating the presence of an active continental margin to the southwest, and subduction from NE to SW (present-day configuration). This magmatic framework is a continuation to the south of what is described for the São Luís cratonic fragment to the north, and the orogenic scenario is identical to what is observed for the same period in the West African Craton (Eburnean/Birrimian orogen), which additionally supports previous geological correlations. In the Neoproterozoic, a few magmatic occurrences are recognized. An extensional event allowed the intrusion of an anorogenic, nepheline syenite at ca. 730 Ma, which was followed by the intrusion of a crustal, calc-alkaline microtonalite, of uncertain tectonic setting, at 624 Ma. Both intrusions underwent greenschist to amphibolite facies metamorphism between 580 and 529 Ma. This metamorphic event is probably related to crustal thickening, which produced crustal melting and intrusion of two-mica granites between 595 and 549 Ma. The absence of oceanic and arc-related assemblages, along with geophysical information about the basement of the Phanerozoic cover indicates an intracontinental setting for the Neoproterozoic–Early Cambrian evolution of the Gurupi Belt, with rifting and posterior closure of the basin, without oceanization. Rifting and closure correlate in time with the onset of Rodinia breakup and West Gondwana assembly, respectively, but we interpret the events in the Gurupi Belt as having no direct role in these two global supercontinent-related events, but, instead, as being related to orogenic events occurring in the periphery of the West African and Amazonian cratons at that time.

## 1. Introduction

The Rhyacian period (2300–2050 Ma) of the Paleoproterozoic Era witnessed the most voluminous crustal growth in South America (Sato and Siga Jr., 2000), and this pattern is also a global phenomenon (e.g., Condie, 1997). The Rhyacian terranes, composed mostly of calc-alkaline

* Corresponding author. Geological Survey of Brazil - SBN, Quadra 02, Bloco H, Ed. Central Brasília, 1° andar, Asa Norte, Brasília, DF, CEP: 70040-904, Brazil.
*E-mail address:* evandro.klein@cprm.gov.br (E.L. Klein).
Peer-review under responsibility of China University of Geosciences (Beijing).

https://doi.org/10.1016/j.gsf.2020.02.016
Received 29 April 2019; Received in revised form 8 January 2020; Accepted 28 February 2020
Available online xxxx
1674-9871/© 2020 China University of Geosciences (Beijing) and Peking University. Production and hosting by Elsevier B.V. This is an open access article under the CC BY-NC-ND license (http://creativecommons.org/licenses/by-nc-nd/4.0/).

Please cite this article as: Klein, E.L. et al., Rhyacian and Neoproterozoic magmatic associations of the Gurupi Belt, Brazil: Implications for the tectonic evolution, and regional correlations, Geoscience Frontiers, https://doi.org/10.1016/j.gsf.2020.02.016

granitoids and metavolcano-sedimentary (greenstone-like) sequences, resulted from the evolution of major accretionary and collisional belts and make up significant portions of Precambrian blocks that form the core of the modern continents (e.g., Amazonia – Santos et al., 2003; Brito Neves and Fuck., 2014; West Africa – Grenholm et al., 2019; Fennoscandia – Petersson et al., 2013). The Neoproterozoic Era (1000–541 Ma), in turn, was characterized, among other features, by the fragmentation of the Rodinia supercontinent (Cawood et al., 2016) followed by the assembly of Gondwana, with suturing of Archean–Paleoproterozoic continental blocks by thousands of kilometers of linear belts (e.g., Meredith et al., 2017; Schmitt et al., 2018 and references therein).

The Gurupi Belt (Almeida et al., 1976), located in north-northwest South America, and with relatively reduced exposed dimensions (160 km-long and 50 km-wide), crops out as a tectonic and erosive window within the Phanerozoic cover (Fig. 1). Aspects of the geological evolution and gold metallogeny have been addressed in the last decade (e.g., Klein et al., 2005a, 2012; Palheta et al., 2009; Klein, 2014, and references therein). These works have demonstrated that almost all of the known lithological framework of the belt at that time was comprised of Paleoproterozoic (Rhyacian) rocks, which participated in the evolution of the São Luís cratonic fragment in the Rhyacian, and only two small Neoproterozoic intrusions had been recognized so far (Appendix A – available as electronic supplementary data). Yet, isotopic systems with relatively low closure temperature (Rb–Sr, K–Ar) record the widespread influence of events around 600–500 Ma (Klein et al., 2005a and references therein). In consequence, the belt is mostly considered to be a Neoproterozoic–Cambrian mobile belt formed at the (present-day configuration) south-southeastern margin of the São Luís-West African cratonic block (Fig. 1) during the Brasiliano/Pan-African cycle of orogenies (Hurley et al., 1967; Almeida et al., 1976; Torquato and Cordani, 1981; Hasui et al., 1984; Lesquer et al., 1984; Klein et al., 2005a, 2012; Klein and Moura, 2008). However, this dichotomy between the poverty in Neoproterozoic rocks and the isotopic evidence raises the question about the tectonic meaning of the Gurupi Belt, i.e., what kind of orogen does it represent and what is the role it played, if any, in continental and supercontinent assembly and dispersion? Past and recent interpretations usually consider Gurupi as a collisional belt (Costa and Hasui, 1997; Costa, 2000; Ribeiro, 2002; Klein et al., 2005a; Palheta et al., 2009), a shear belt (Pastana, 1995; Klein and Moura, 2003), or aulacogen (Cordani et al., 2013).

With direct implications on this major issue, several other questions remain unsolved or deserving additional discussion. These include: (1) The juvenile, calc-alkaline, Rhyacian (2168–2147) granitoids, which form an important part of the São Luís cratonic fragment (Tromaí Intrusive Suite), are relatively well characterized in the cratonic area with respect to their magmatic evolution and tectonic setting (Klein et al., 2008). This suite also crops out within the Gurupi Belt in close spatial association with "basement" gneisses and metamorphosed granitoids (Fig. 2). Do these gneisses and metagranitoids represent deformed and metamorphosed equivalents of the Tromaí Intrusive Suite, as suggested by Gorayeb et al. (1999), or do they record coeval but distinct magmatic episodes? (2) What is the age and magmatic/tectonic setting of the small mafic (amphibolite) and granitoid plutons described in recent geological mapping surveys (Klein and Lopes, 2011, 2017)? (3) What is the tectonic setting of the metavolcano-sedimentary Chega Tudo Formation (~2160 Ma; Fig. 2), which is the main host for the orogenic gold deposits in the belt (Klein, 2014)? (4) Considering that two episodes (~2100 Ma and ~549 Ma) of strongly peraluminous, collision-type granite magmatism have already been recorded in the belt (Villas and Sousa, 2007; Palheta et al., 2009; Klein et al., 2012), to which one, if any, are related the several bodies of the undated "undifferentiated" peraluminous granites described in Klein et al. (2015)? (5) What are the ages of metamorphism and deformation recorded in the Gurupi Belt?

In order to address some of these issues and bring a new understanding about the evolution, regional and global significance of the Gurupi Belt, including supercontinent assembly and breakup, in this

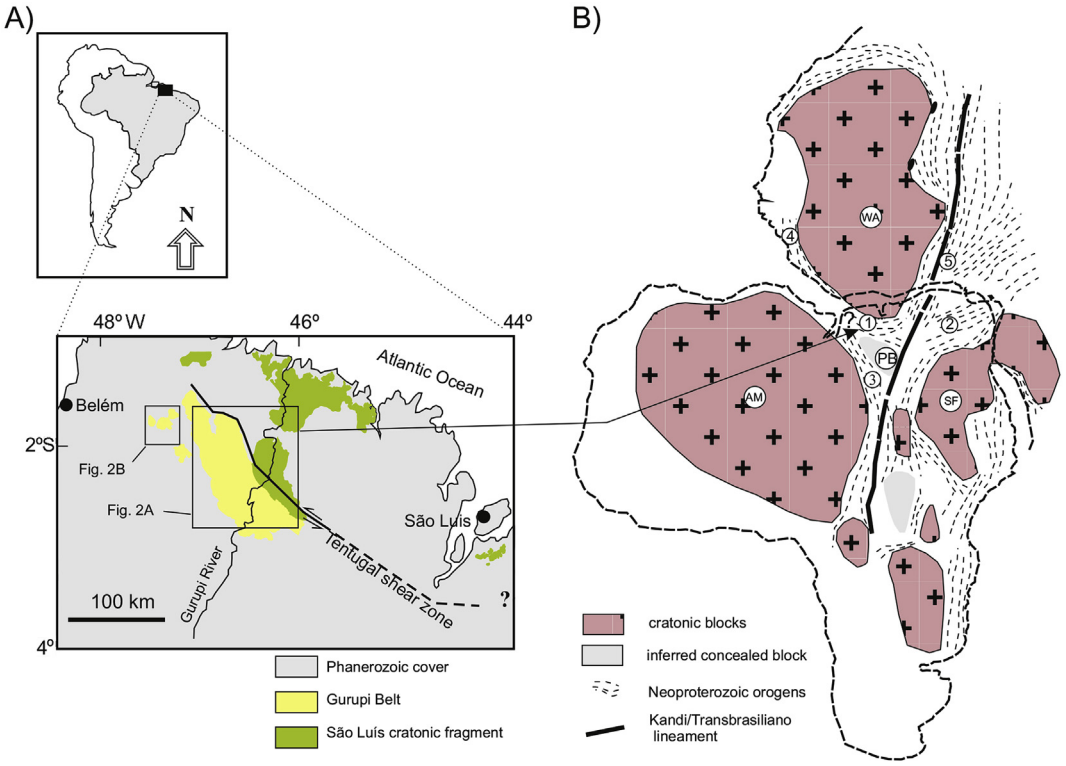


**Fig. 1.** (A) Location map of the exposed portions of the Gurupi Belt and São Luís cratonic fragment. (B) Cartoon not to scale showing the cratons (WA: West African-São Luís Craton; AM: Amazonian Craton; SF: São Francisco Craton; PB: Parnaíba block) and Neoproterozoic mobile belts (1: Gurupi; 2: Borborema; 3: Araguaia; 4: Rockelide; 5: Dahomeyde) of South America and West Africa (modified from Klein and Moura, 2008).

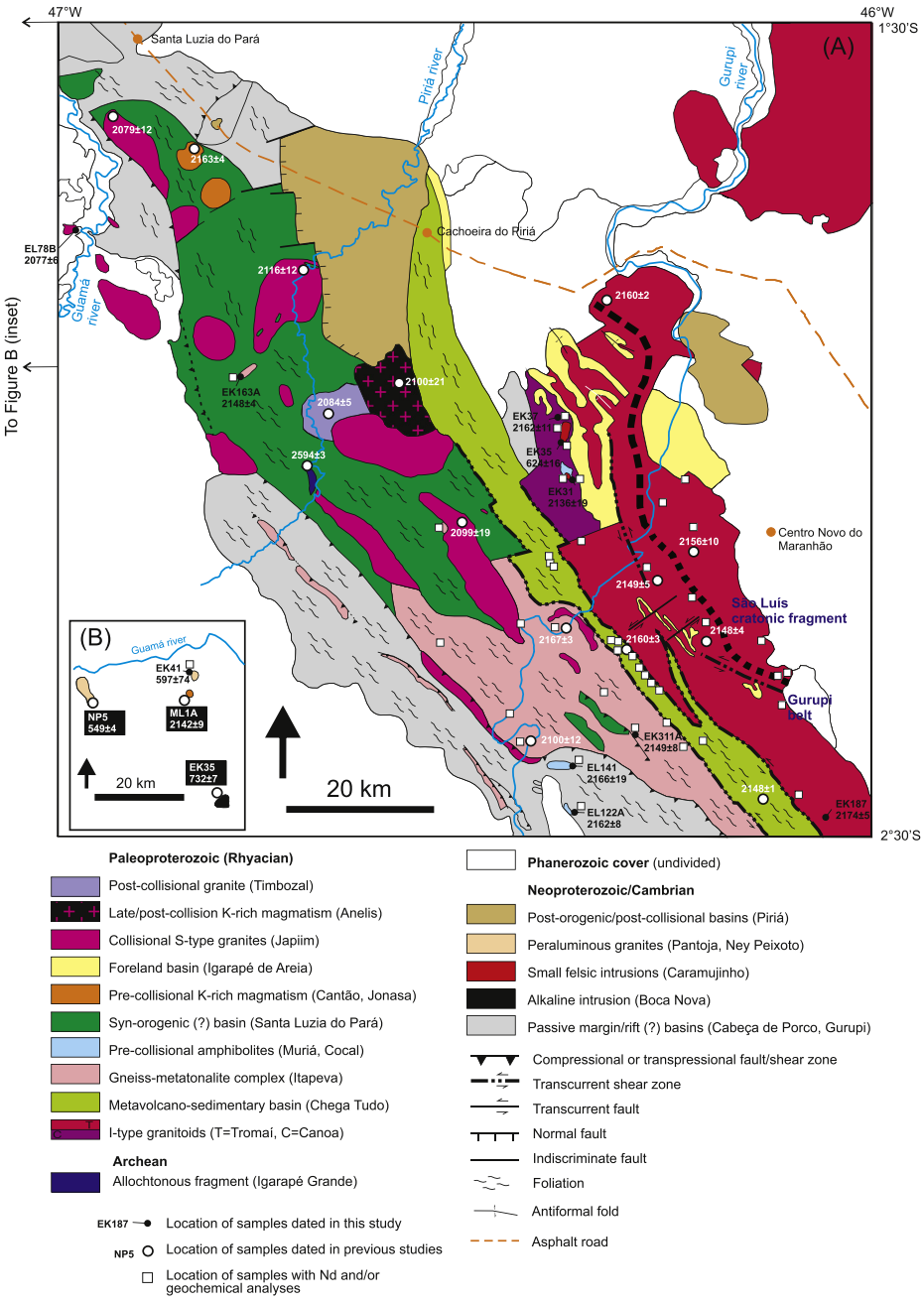


**Fig. 2.** (A) Geological/tectonic associations map of the Gurupi Belt, with stratigraphic names used in the text given in parentheses. (B) Simplified geological map (inset) showing the location of small igneous bodies cropping out within the Phanerozoic cover, in the western portion of the Gurupi Belt (outside the main map). Sampling locations of the samples dated in this and in previous studies are indicated. Locations of the samples with Nd and/or geochemical analyses are also indicated.

study we investigate the age of crust and rock formation, metamorphism, deformation, and the geochemical characteristics of magmatic associations, which straddles the supposed tectonic boundary (Tentugal Shear Zone) between the Gurupi Belt and the São Luís cratonic fragment (Fig. 1). We make use of extensive geological mapping supported by high-resolution airborne geophysics, including the acquisition of new and reinterpretation of available structural and petrographic data, and bring new in situ U–Pb zircon geochronological information, along with whole-rock Nd and geochemical data.

## 2. Geotectonic context

The Gurupi Belt forms part of the basement of the Parnaíba tectonic province, in the sense of Almeida et al. (1981), and crops out as a tectonic and erosive window within the Phanerozoic cover. It is consensual that this belt integrated a continental mass (West Gondwana) that became part of the South America continent after the break-up of the Pangea supercontinent (Hurley et al., 1967; Torquato and Cordani, 1981; Lesquer et al., 1984; Klein and Moura, 2008 and many others). As a consequence, the southern portion of the West African Craton, the eastern Amazonian Craton (Carajás and Bacajá domains, SE-Guyana shield), and the Brasiliano/Pan-African mobile belts (Araguaia and Borborema in Brazil, Rockelide and Dahomeyide in Africa) were likely the surroundings of the Gurupi Belt in the beginning of the Phanerozoic Era (Fig. 1).

Most of the boundaries of the Gurupi Belt, including the Araguaia Belt to the west, the Borborema Province to the east, and the inferred Parnaíba block to the south (Fig. 1), are concealed beneath the Phanerozoic basins and have been interpreted using seismic, gravity and magnetic

data (Brito Neves et al., 1984; Nunes, 1993; Castro et al., 2014; Daly et al., 2014). The exposed Tentugal Shear Zone represents only a Rb–Sr and K–Ar geochronological limit between the Gurupi Belt and the São Luís cratonic fragment (Klein et al., 2005a, 2012 and this study), and not a tectonic boundary or suture zone (e.g., Hasui et al., 1984; Abreu and Lesquer, 1985; Castro et al., 2014). A tectonic boundary, possibly a suture zone, was inferred (Oliveira, 2016) to be located approximately in the intermediate portion between positive and negative gravity anomalies, about 50 km southwest of the outcropping area of the Gurupi Belt.

### 2.1. São Luís cratonic fragment: summary of the geology

Given the physical continuity between the Gurupi Belt and the São Luís cratonic fragment (Fig. 1), a summary of the geological evolution of the latter is presented here (details in Pastana, 1995; Klein et al., 2005b, 2008, 2009, 2014; Palheta et al., 2009; Nogueira et al., 2017). The cratonic fragment is composed of rocks formed from 2240 to 2009 Ma. The oldest known association comprises the island arc-related metavolcano-sedimentary sequence (Aurizona Group, 2240 ± 5 Ma), which was intruded by shallow granophyric rocks at ca. 2214 ± 3 Ma. Batholiths and stocks of juvenile, subduction-related, metaluminous to slightly peraluminous calc-alkaline granitoids of the Tromaí (2168 ± 4 to 2147 ± 3 Ma) and Rosário (2170 ± 7 to 2161 ± 4 Ma) intrusive suites, which developed in island and magmatic arcs, also intruded the metavolcano-sedimentary sequence. Andesite, dacite and subordinately basic volcanic rocks of 2164 ± 3 Ma (Serra do Jacaré volcanic unit), formed in mature arc with minor back-arc component. Minor coeval calc-alkaline felsic volcanic rocks and tuffs of 2160 ± 7 Ma (Rio Diamante Formation), with limited Archean inheritance formed in a continental margin. The peraluminous, collision-type magmatism of 2086–2091 Ma (Tracuateua Suite) was followed by the emplacement of post-orogenic/post-collisional, highly evolved/shoshonitic granite (Negra Velha Granite) of 2056–2076 Ma, isolated bodies of felsic volcanic and tuffaceous rocks of 2068 Ma (Rosilha volcanic unit), and the late, small, shallow intrusion of calc-alkaline tonalite (Caxias microtonalite) dated at 2009 ± 11 Ma.

### 2.2. Gurupi Belt: summary of the geology

The geological framework of the Gurupi Belt (Fig. 2) comprises igneous, sedimentary and metamorphic rock units of variable natures with ages ranging from 2695 Ma to 549 Ma (Klein and Moura, 2001; Klein et al., 2005a, 2012; Palheta et al., 2009). Many of these rock units follow the general northwest-southeast tectonic trend in the belt (Fig. 2). The oldest known unit is the Archean Igarapé Grande metatonalite, of 2695 ± 4 Ma. However, most of the units consist of rocks formed during the same period of crustal growth and recycling recorded in the São Luís cratonic fragment, approximately between 2240 Ma and 2000 Ma (Appendix A). In fact, Klein et al. (2012) interpreted several granitic suites as remnants of disrupted blocks that may represent an active margin and/or collision belt associated with a Rhyacian orogeny. The Rhyacian units include foliated to banded gneisses of 2167 ± 3 Ma (Itapeva Complex, which will be detailed below); batholiths of the juvenile calc-alkaline granitoids of the Tromaí Intrusive Suite (2165 ± 8 to 2148 ± 4 Ma); the juvenile, 2160 ± 3 to 2146 ± 1 Ma-old metavolcano-sedimentary Chega Tudo Formation; different generations of potassic biotite-bearing calc-alkaline and weakly peraluminous granitoids of 2163 ± 4 Ma (Cantão), 2142 ± 9 Ma (Jonasa), and 2084 ± 5 Ma (Timbozal), with crustal signature; several generations of variably deformed peraluminous, muscovite- and biotite-bearing granites and leucogranites with ages between 2116 Ma and 2072 Ma and remarkable crustal signature (Moça, Maria Suprema, Japiim, Tamancuoca and other undated plutons); a highly evolved/shoshonitic granite to quartz-syenite pluton of 2100 ± 21 Ma (Anelis Suite); a siliciclastic sequence younger than 2078 Ma (Igarapé de Areia Formation); and undated gabbroic and amphibolite intrusions (Klein et al., 2005a, 2012; Palheta et al., 2009, and references therein).

Neoproterozoic units comprise siliciclastic metasedimentary rocks younger than 1140 Ma (Gurupi Group) and 630 Ma (Piriá Formation), an anorogenic/pre-orogenic silica-undersaturated peralkaline intrusion of 732 ± 7 Ma that has subsequently been deformed and metamorphosed to amphibolite facies conditions (Boca Nova Nepheline Syenite); and the peraluminous, two-mica granite (Ney Peixoto Granite) of 549 ± 4 Ma (Klein et al., 2005a; Palheta et al., 2009).

### 2.3. Main structural features in the Gurupi Belt

Tavares et al. (in review) described three sets of ductile and ductile-brittle structures, according to crosscutting relationships they show in rocks formed in Paleoproterozoic and Neoproterozoic times, along with late brittle structures. (1) $D_1$ was recognized only in Rhyacian units, such as the Itapeva Complex and the ca. 2100 Ma-old two-mica granites; it was interpreted to be coeval to this collision-type magmatism and associated with lower greenschist to upper amphibolite metamorphic conditions. A steep, fine to coarse anastomosed foliation ($S_1$) was produced in this phase, striking predominantly to N40°–50°W, with a down-dip (SW) lineation. The $S_1$ foliation was crenulated and progressively and coaxially folded by $D_{1b}$. Widespread orogenic gold mineralization is associated with this phase. (2) $D_2$ also affected only Paleoproterozoic units and is characterized by ductile-brittle $S_2$ structures, which define open to tight folding, discrete shear bands and the crenulation of the $S_1$ schistosity observed in the supracrustal sequences. $S_2$ strikes WNW–ESE to E–W, and dip variably to NNE, NNW, SSE, and SSW. Orogenic gold mineralization is also associated with this phase. (3) $D_3$ is present in both Neoproterozoic and Paleoproterozoic units; the $S_3$ structures consist of slaty cleavage, crenulation, and asymmetric folding, with S-dipping axis, developed under greenschist to amphibolite conditions, with direction averaging N–S.

The left-lateral strike-slip Tentugal shear zone (TSZ), perhaps the most striking lineament in the Gurupi Belt, is regarded as the geochronological boundary between the São Luís cratonic fragment and the Gurupi Belt (Klein et al., 2005a), and not as a suture (e.g., Hasui et al., 1984). Hasui et al. (1984) suggested that the TSZ has been active both in the Paleoproterozoic and Neoproterozoic times, which is in line with the recent interpretation of Tavares et al. (in review). Tavares et al. (in review) considered that the development of the TSZ is coeval to the Paleoproterozoic $D_1$ and that it was reactivated in shallower depth as a transpressional zone during to the Neoproterozoic $D_3$.

## 3. Analytical procedures

Concentrates of zircon and titanite for U–Pb analysis were obtained by crushing the rock and then sieving, panning and using a magnetic separator and dense liquids. Zircon crystals were hand-picked under a binocular microscope, mounted in epoxy resin, and polished with diamond paste. Cathodoluminescence (CL) and/or backscattered electron (BSE) imaging, followed by conductive gold coating preceded the analyses.

The U–Pb LA-ICP-MS analyses were undertaken at the Laboratório de Estudos Geocronológicos, Geodinâmicos e Ambientais of the Universidade de Brasília (UnB), Brasília, Brazil, and one sample was analyzed in the Laboratório de Geologia Isotópica of the Universidade Federal do Rio Grande do Sul, in Porto Alegre, Brazil. In both laboratories, the analyses followed procedures described in detail in Bühn et al. (2009). The analyses were performed with a Thermo Finnigan Neptune multi-collector inductively coupled plasma mass spectrometer with an attached New Wave 213 μm Nd-YAG solid-state laser. The laser parameters include spot size of 30 μm, frequency of 10 Hz, and energy fluence of 2 J/cm$^2$, except for samples EL122A and EK141 (~14 J/cm$^2$, necessary because the determination of the $^{206}$Pb isotope was via Faraday detector). The acquisition followed a standard – sample bracketing technique with four sample analyses between a blank and a GJ-1 zircon standard. The accuracy was controlled using the standard zircon UQ-Z (1143 ± 11 Ma – Machado and Gauthier, 1996) or

PAD (688 ± 2 Ma – Rosa et al., 2003), as detailed in Appendix B. The common lead contents ($Pb_c$) were determined using the measured $^{204}Pb$ and by applying the Pb evolution model of Stacey and Kramers (1975). The $^{202}Hg$ was used to correct the $^{204}Hg$ isobaric interference. Due to the inaccuracy in the determination of this value, no correction for isotopic ratios was applied, except for the titanite sample (EL141). For most of the samples, this parameter was used to exclude analyses only in case where it was very high. In the absence of a proper standard, the titanite analyses were normalized within the zircon runs. Raw data were reduced using an in-house program and corrections were done for background, instrumental mass-bias drift and common Pb, as described in Bühn et al. (2009). The ages were calculated using ISOPLOT 3.0 (Ludwig, 2003), and data are reported following recommendations of Horstwood et al. (2016).

The U–Pb SIMS analyses were undertaken on SHRIMP II and RG of the Research School of Earth Sciences of the Australian National University (ANU), Canberra, Australia, and at the Centro de Pesquisas Geocronológicas of the University of São Paulo (IGc-CPGeo-USP), Brazil, using a SHRIMP-IIe, in both cases following the methods described in Compston et al. (1984) and Williams (1998). At ANU, the zircon crystals were mounted in epoxy, together with the reference zircons TEMORA-1 (Black et al., 2003) and FC1 (Paces and Miller, 1993), whereas the SL13 standard (a chip of a single crystal with a uniform U content) was used to calibrate U, Th and Pb concentrations. At USP, the crystals were mounted, together with the TEMORA-2 standard (Black et al., 2004). Analyses of secondary zircon standard (Z6266) was used to verify the accuracy of the U–Pb calibration, and the age of 566 ± 4 Ma was obtained in this session. Uranium abundance and U/Pb ratios were calibrated against the TEMORA standard. In both laboratories, correction for common Pb was made based on the $^{204}Pb$ measured, and the typical error for the $^{206}Pb/^{238}U$ ratio is less than 2%. Age calculations and concordia plots were done using Isoplot/Ex software (Ludwig, 2003).

Analyses for individual spots are plotted on concordia diagrams with $2\sigma$ uncertainty. Where data are combined to calculate an age, the quoted uncertainties are at 95% confidence level, with uncertainties in the U–Pb standard calibration included in any relevant U–Pb intercept and concordia age calculations.

Sm–Nd analyses were undertaken at the UnB using analytical procedures described in Gioia and Pimentel (2000). Accordingly, 50 mg of whole rock powders were mixed with a $^{149}Sm/^{150}Nd$ spike and dissolved in Savilex vessels. The Sm–Nd separation used cation exchange Teflon columns with Ln-Spec resin, then Sm and Nd were deposited in Re filaments and the isotopic ratios were determined on a FINNIGAN MAT 262 mass spectrometer using the static mode. The Nd data were normalized to a $^{146}Nd/^{144}Nd$ ratio of 0.7219 and uncertainties in the Sm/Nd and $^{143}Nd/^{144}Nd$ ratios were about 0.4% ($1\sigma$) and 0.005% ($1\sigma$), respectively, based on repeated analysis of the BHVO-1 standard (Appendix B). The crustal residence ages were calculated using the values of DePaolo (1988) for the depleted mantle ($T_{DM}$).

Major and trace elements were analyzed by ICP-ES and ICP-MS, respectively, at the Acme Analytical Laboratories Ltd. in Canada, and at the SGS Geosol lab in Brazil, following equivalent procedures, which involve Li metaborate/tetraborate fusion. Chemical diagrams were mostly produced using the GCDkit software (Janousek et al., 2006).

## 4. Magmatic associations of the Gurupi Belt

This paper focuses on the Rhyacian and Neoproterozoic magmatism. The Archean, 2594 ± 3 Ma-old Igarapé Grande Metatonalite (Fig. 2) described and dated by Klein et al. (2005a) is a small and allochthonous basement fragment, of unknown provenance, and will not be further addressed here. Below we describe the different magmatic associations (including information from this work and available in the literature), in terms of field and petrographic aspects, and geochemistry. Photomicrographs, and chemical results are available as electronic supplementary data (Appendices C and D, respectively).

### 4.1. Rhyacian gneiss-metatonalite complex

#### 4.1.1. Field and petrographic characteristics

Gneisses, metatonalite bodies and isolated outcrops of mafic-ultramafic rocks were grouped in the Itapeva Complex (Klein et al., 2005a; Klein and Lopes, 2011). The main occurrence of this complex is an elongated, NW–SE-trending massif that crops out from the centre to the southeastern limit of the exposed Gurupi Belt (Fig. 2). This massif occurs in tectonic contact with the metavolcano-sedimentary Chega Tudo Formation along the left-lateral strike-slip Tentugal Shear Zone, and with granitoids and Neoproterozoic supracrustal units to the southwest along thrust faults (Fig. 2). Smaller, isolated bodies of gneisses occur towards the northwestern portion of the belt, in tectonic contact with Paleoproterozoic supracrustal sequence (Fig. 2).

The foliation in the gneisses is defined by the alternation of mafic and quartzo-feldspathic layers (Fig. 3A), which corresponds to the $D_1$–$S_1$ phase described by Tavares et al. (in review). This foliation was progressively and coaxially crenulated and folded in a $D_{1b}$ event. Complex refolding and interference structures associated with local migmatization have been observed at least locally. Relicts of isoclinal folds locally appear sandwiched between the foliated gneisses, likely resulting in the commonly observed banding that also strikes parallel to the $S_1$ foliation, and apparently forming a composed $S_1 + S_{1b}$ structure. Sheets of peraluminous, muscovite-bearing (collision-type) granites intruded into the gneisses during $D_1$, i.e., about 2100 Ma, as already suggested by Klein et al. (2005a). We have also observed disrupted quartz, quartzo-feldspathic, and leucogranite veins (migmatization) within the foliation planes, which have been folded coaxially to the gneisses ($D_{1b}$). One of these veins furnished an age of 2090 ± 20 Ma (Klein and Moura, 2003), which is similar to the age of the peraluminous granites.

Originally, only orthogneisses have been included in the Itapeva Complex by Klein et al. (2005a). These grey and medium-grained rocks are indeed the predominant types, but subordinate occurrences of metatonalites and paragneisses have also been identified in this work. The distinction between the different types of gneisses is not straightforward. In general, it is only possible with petrographic and/or geochemical support. Locally, metagranitoids and mafic-ultramafic rocks appear as isolated and discontinuous outcrops and could neither be separated as individual units nor related to other known units. Therefore, these rocks remained included in the complex, but they are not further addressed in this study. Quartz feldspathic mobilized and granitic veins are frequent. The presence of quartzose and granitic mobilized and local migmatization suggest that partial melting has been achieved during metamorphism under amphibolite facies conditions.

Most of the orthogneisses are biotite- and epidote-biotite gneisses having tonalite and quartz diorite composition. Depending on the composition of the protolith, these rocks are formed by plagioclase (45%–56%), quartz (25%–30%), microcline (4%–5%, locally absent), and biotite (11%–20%). Neoformed, coarse-grained and zoned epidote (4%–5%) is ubiquitous, but it also occurs as fine-grained alteration mineral in close association with sericite and chlorite and, in places, with carbonate. Opaque minerals (mostly magnetite), apatite, and zircon are the main accessory phases. Allanite and garnet occur occasionally.

A subordinate compositional type comprises hornblende- (±biotite) bearing tonalite to granodiorite and quartz monzodiorite gneisses. The rocks are composed of plagioclase (40%–61%), quartz (15%–27%), microcline (10%–12%, but absent in tonalites), hornblende (5%–30%), and biotite (3%–7%, but absent in some samples). Epidote, titanite, opaque minerals, zircon, apatite and allanite are accessory phases.

All orthogneisses are predominantly granoblastic and lepidoblastic. The plagioclase-biotite-amphibole paragenesis indicates metamorphism under amphibolite facies conditions, which is additionally indicated by migmatization. Chloritization of biotite and amphibole indicates retrograde greenschist metamorphic conditions. Mylonitic and porphyroclastic textures are common and we have also observed evidence of dynamic deformation overprinting the metamorphic minerals.

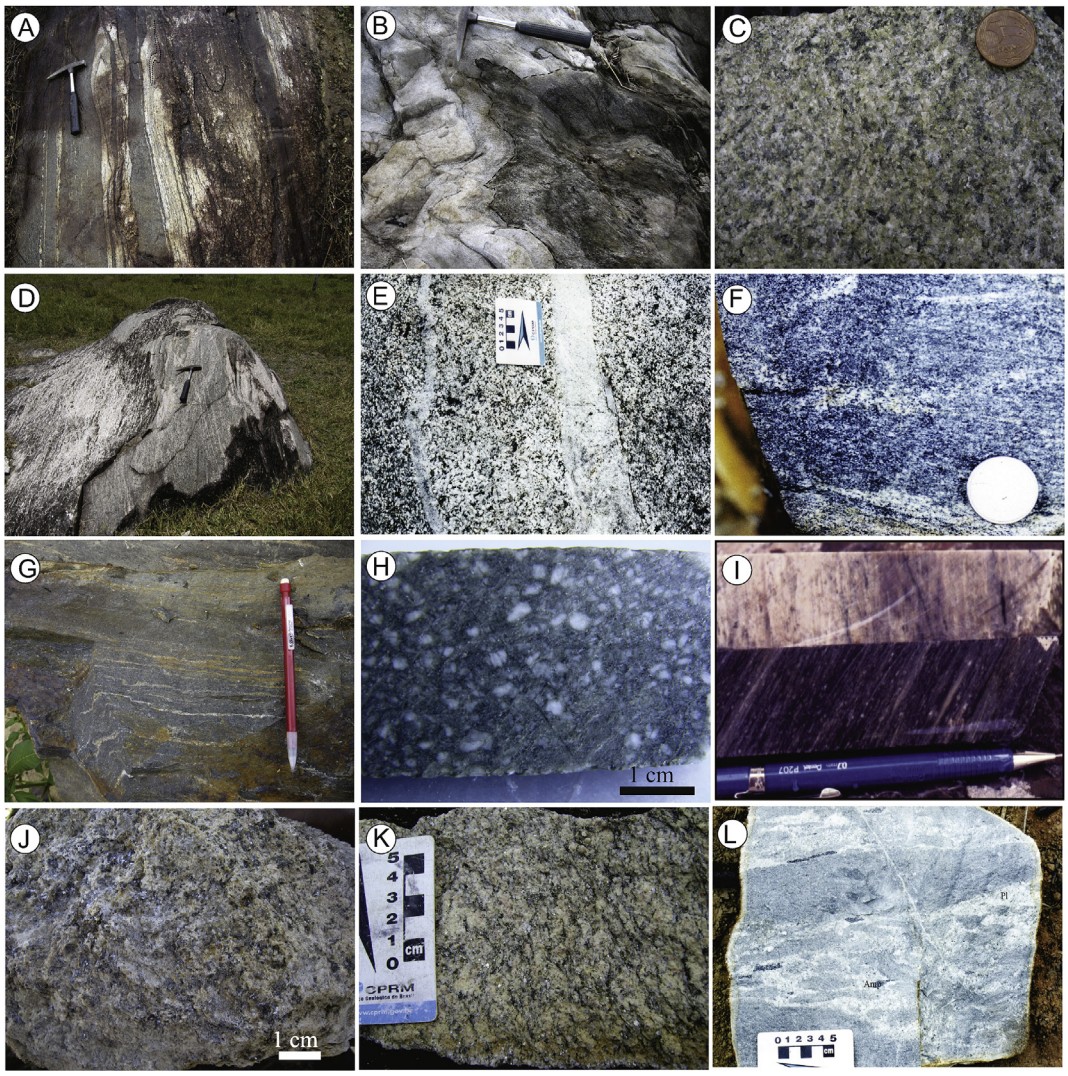


**Fig. 3.** Representative outcrop pictures of magmatic rocks of the Gurupi Belt. Rhyacian gneiss-metatonalite complex (Itapeva Complex): (A) Gneiss with mafic and felsic bands showing isoclinal folding. The dashed lines outline asymmetric shear folds indicating dextral movement; (B) Metatonalite (light grey) intruding metasedimentary schist (dark grey). Rhyacian calc-alkaline high Ba–Sr granitoids (Tromaí Intrusive Suite); (C) Chloritized and saussuritized equigranular tonalite; (D) Foliated grey granodiorite cut by veins of syenogranite. Rhyacian ferroan granitoid: (E) Grey, coarse-grained quartz diorite of the Canoa unit, cut by quartz veins. Rhyacian amphibolite units: (F) Compositional banding of the Muriá amphibolite, with plagioclase- and amphibole-rich bands (the coin diameter is 2 cm); (G) Folded compositional banding of the Cocal amphibolite. Rhyacian volcanic and metavolcanic rocks of the Chega Tudo Formation: (H) Undeformed andesite porphyry, with plagioclase phenocrysts; (I) Deformed (mylonitized) dacite porphyry. Peraluminous granites: (J) Coarse-grained two-mica syenogranite (Japiim Suite); (K) Foliated muscovite-rich syenogranite of the Pantoja unit. Neoproterozoic calc-alkaline intrusion: (L) Metamicrotonalite of the Caramujinho unit. The locally banded aspect is given by portions enriched in plagioclase and stretched mafic enclaves.

The metatonalites occur in close spatial association with the gneisses, but they are predominant in the SE tip of the main massif. The rocks are grey, medium-grained and normally foliated, and contain decimeter-long pods/enclaves of more felsic tonalite and lenses (boudins) of disrupted quartz veins. The enclaves are strongly elongated and parallel to the $S_1$ foliation. Sharp and irregular intrusion relationships with a muscovite-biotite-schist are clearly observed (Fig. 3B). Compositionally, the rocks are biotite- to epidote-biotite-metatonalites. Primary textures are locally preserved, except for the development of incipient mylonitization. No compositional layering has been observed. The mineralogical composition consists of plagioclase (40%–52%), quartz (25%–34%), K-feldspar (0–4%), biotite (15%), epidote (4%–8%) and trace amounts of garnet, opaque minerals, zircon, and apatite. Muscovite, chlorite, and carbonate are alteration phases.

*4.1.2. Geochemistry*

Both orthogneisses and metatonalites are calc-alkaline and weakly to moderately peraluminous rocks (Fig. 4A and B). The orthogneisses are low- to medium-K rocks and have $SiO_2$ (acidic rocks), Sr, Co, Ga, Sc, Hf, Nb, V, Y and Zr contents higher than those presented by the metatonalites. The REE pattern is fractionated, with $(La/Yb)_n$ ratios ranging from 9.0 to 14.3, and weak negative to positive europium anomalies are given by Eu/Eu* ratios of 0.83–1.19 (Appendix D and Fig. 5A). The trace element distribution shows enrichments relative to the primitive mantle, fractionation between LILE and HFSE, negative anomalies of Nb, P and Ti, and slightly positive Sr anomalies (Fig. 5B). This pattern is typical of calc-alkaline suites, and the negative Nb anomaly and the low Nb and Ta concentrations are consistent with derivation from subduction-related magmas. Furthermore, the anomalies may be ascribed, at least in part, to local accumulation of plagioclase (Sr) and fractional crystallization involving Fe–Ti oxides.

The metatonalites are intermediate rocks with $Al_2O_3$, $Na_2O$ and $K_2O$ concentrations higher than those of orthogneisses. The Hf (<0.35 ppm), Nb (<1.37 ppm), Sr (<14 ppm), and Zr (<4.4 ppm) contents of the

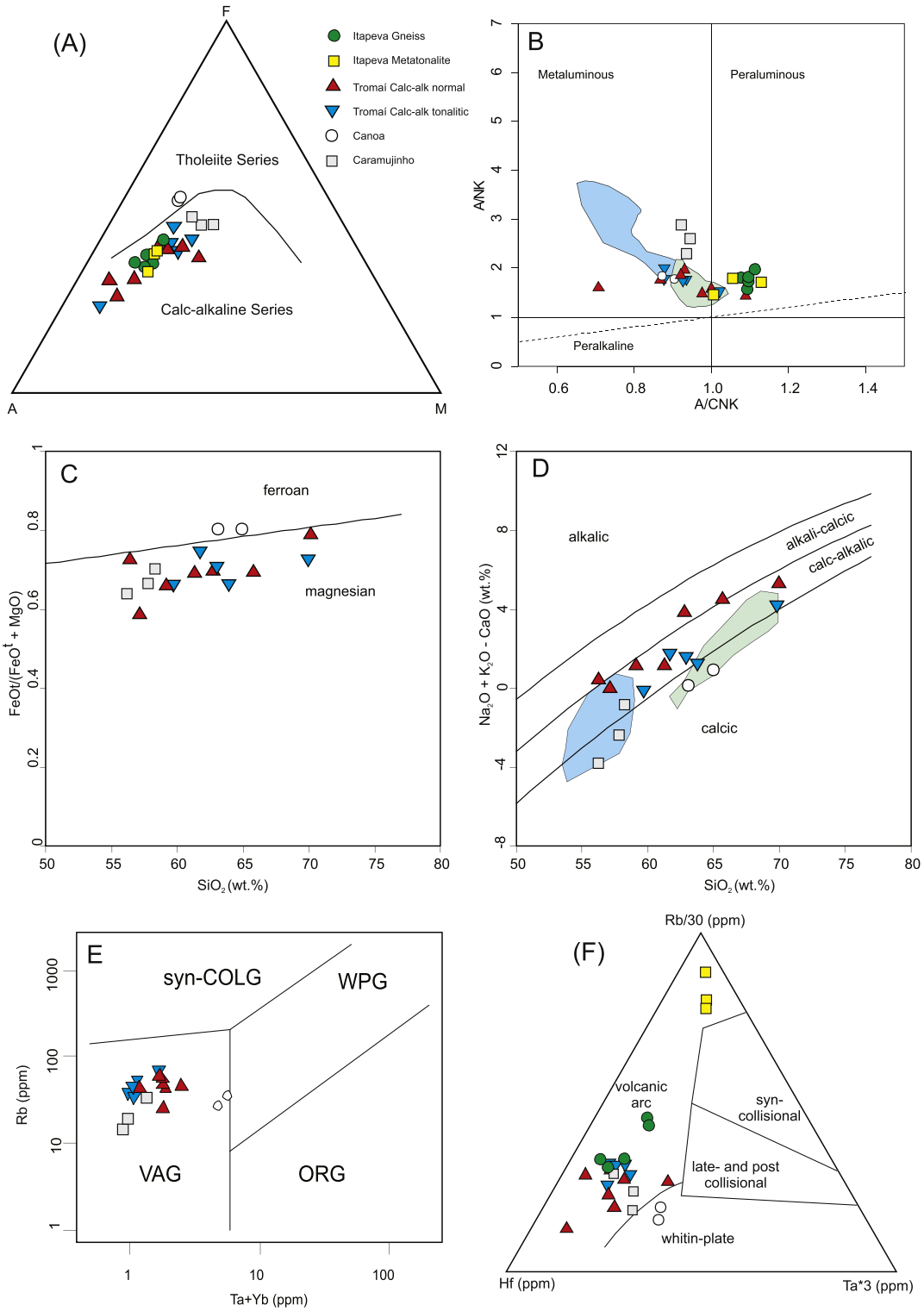


**Fig. 4.** Geochemistry of Rhyacian and Neoproterozoic gneiss and granitoid units: Itapeva Complex, Tromaí Suite, Canoa quartz diorite, and Caramujinho metamicrotonalite. (A) AFM diagram of Irvine and Baragar (1971). (B) A/CKN vs. A/NK (Shand diagram). (C) $SiO_2$ vs. $FeO^t/(FeO^t + MgO)$ and (D) $SiO_2$ vs. $K_2O + Na_2O - CaO$ (Frost and Frost, 2001). The fields of the tonalitic (blue) and granodioritic (green) varieties of the Tromaí Suite of the São Luís cratonic fragment (Klein et al., 2008) are represented for comparison. Tectonic discriminant diagrams: (E) Rb vs. Ta + Yb plot of Pearce et al. (1984); (F) Rb/30 – Hf – Ta × 3 triangular plot of Harris et al. (1986).

metatonalites are very low. In addition to different elemental concentrations, the metatonalites show REE distribution, in average, less fractionated than the orthogneisses, with $(La/Yb)_n$ varying between 4.8 and 11.3 (Appendix D and Fig. 5B). Europium anomaly is absent to weakly positive (Eu/Eu* = 1.00–1.19), suggesting accumulation of plagioclase during magmatic evolution. LILE and HFSE are also enriched in relation to the primitive mantle and fractionated. The most significant difference in comparison with the orthogneisses is the deeper Nb negative anomaly and the presence of pronounced Sr and Zr, and moderate Y, negative breaks, which are absent in the orthogneisses (Fig. 5B). These

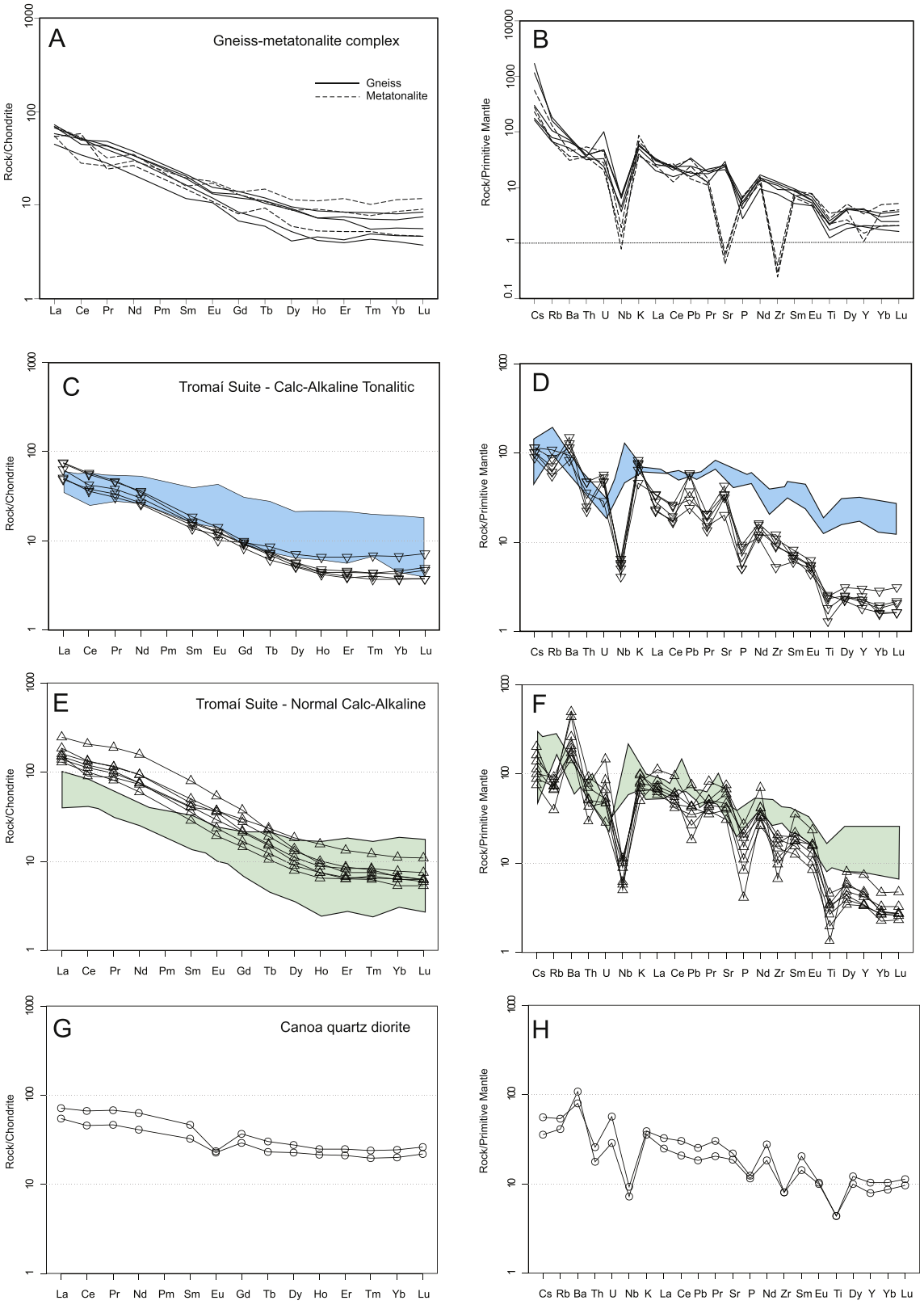


**Fig. 5.** Chondrite-normalized REE and primitive mantle-normalized diagrams for Rhyacian gneiss and granitoid units. Normalization according to Boynton (1984), and Sun and McDonough (1989), respectively. (A and B) gneiss-metatonalite complex (Itapeva Complex), (C–F) high Ba–Sr (Tromaí Suite), and (G, H) ferroan (Canoa) granitoids. For comparison, the fields of the tonalitic (C, D) and granodioritic (E, F) varieties of the Tromaí Suite of the São Luís cratonic fragment (Klein et al., 2008) are represented.

characteristics are also consistent with those of subduction-related magmas but indicate that metatonalites and orthogneisses formed from different magma sources and/or magmatic processes. The Sr behavior in the metatonalites is admitted to result from fractionation of plagioclase (combined with Sr loss during alteration-albitization of plagioclase). However, this contrasts with the Eu behavior, which may additionally be a consequence of garnet or amphibole-bearing residues (e.g. Li and Li, 2003). The negative Zr anomaly, associated with low Hf values, probably reflects zircon fractionation. Fractional crystallization of plagioclase + Fe–Ti oxides and zircon might explain small differences in Sr, Zr and some transition elements, but cannot account for the enrichment in REE.

In terms of tectonic setting, the protoliths of orthogneisses and metatonalites plot in the field of volcanic arc granites (Fig. 4F), but there is a clear separation between the two rock types, given by the low Hf contents of the metatonalites, which indicates at least different magma sources for the parental magmas.

### 4.2. Rhyacian calc-alkaline high Ba–Sr and ferroan granitoids

Granitoids and metagranitoids (separation is not straightforward) that form a large and broadly continuous composite batholith in the boundary zone between the Gurupi Belt and the São Luís cratonic fragment (Fig. 2) have been grouped in the Tromaí Intrusive Suite (Pastana, 1995; Klein et al., 2005b; Klein and Lopes, 2011). In this work, and based on geophysical, petrographic, and geochemical characteristics, we consider two different units (Fig. 2): (1) the undivided Tromaí Intrusive Suite, comprising calc-alkaine high-Ba-Sr granitoids, and (2) the Canoa quartz diorite, composed of ferroan granitoids. The two granitoid units are medium- to coarse-grained, massive to foliated rocks, and usually show greenish color (Fig. 3C and D), which is due to metamorphism and/or regional hydrothermal alteration along the Tentugal shear zone. Mafic, and tonalite to quartz diorite microgranular enclaves are common features, and no xenoliths have been observed, which is also a characteristic feature of the Tromaí Suite in the São Luís cratonic fragment (Klein et al., 2008).

A third Rhyacian granitoid unit comprises the Cantão Granite, which crops out as rounded bodies in the northwestern portion of the Gurupi Belt, surrounded by metasedimentary formations (Fig. 2). This is a high-K calc-alkaline granite of 2163 ± 4 Ma, already described elsewhere (Palheta et al., 2009; Klein et al., 2012), which differs from the Tromaí Suite in terms of geochemistry and isotopic composition.

#### 4.2.1. Tromaí Intrusive Suite: petrography and geochemistry

Based on petrographic and geochemical characteristics (Appendix D), two granitoid groups can be broadly defined, although these cannot be separated in map. One group is composed of more primitive rocks that follow a calc-alkaline tonalitic (CAT) magmatic series on the QAP diagram of Streckeisen (1976) (Appendix D), comprising hornblende tonalites and subordinate hornblende granodiorite, both lacking biotite. The other group consists of biotite (±hornblende)-bearing granitoids with more variable petrographic composition, including quartz diorite, quartz monzodiorite, granodiorite, quartz monzonite, and monzogranite. These rocks broadly follow a normal calc-alkaline (CAN) trend (QAP – Appendix D).

The mineralogy of the CAT group consists of plagioclase (38%–53%), quartz (19%–30%), K-feldspar (1%–16%), and hornblende (3%–20%). Titanite (up to 2%), opaque minerals (up to 2%) and traces of zircon and apatite are accessory phases. The CAN rocks contain plagioclase (35%–62%), quartz (10%–23%), K-feldspar (4%–28%), biotite (4%–5%), and hornblende (4%–20%) as essential minerals, along with accessory titanite (up to 2%), opaque minerals (up to 2%), and traces of zircon, apatite, and allanite.

In average, the CAT rocks show slightly higher $SiO_2$ and $Fe_2O_3$ contents, and slightly lower $Al_2O_3$ and $Na_2O$ contents than those of the CAN rocks, which, in turn, show quite higher Ba, Sr, Zr, and Hf concentrations (Appendix D). In addition, the CAT rocks show lower Ba/Rb (average 19), and higher Sr/Y (average 77.5) ratios when compared to those of the CAN granitoids (respectively 41 and 65.4, in average). Both groups form a calc-alkaline, predominantly metaluminous, magnesian, and high Ba–Sr association (Figs. 4 and 6).

A more significant distinction is given by the rare earth elements (Fig. 10A, C). The CAN granitoids show higher REE contents (average 250 ppm) and greater fractionation between light and heavy elements [$(La/Yb)_n$ = 20.7–36.7] than what is presented by the CAT rocks (respectively, 91 ppm and $(La/Yb)_n$ = 13.5–17.9). Both groups lack significant Eu anomalies, indicating a genetic kink with mafic magmas (e.g., Moreira et al., 2018). The general behavior of trace elements (but with variations within individual groups, Fig. 6) is of variable enrichment in relation to the primitive mantle, expressive fractionation between LILE and HFSE, pronounced negative Nb, P, and Ti anomalies, and positive anomalies of Ba, K, and Sr. The CAN group also shows negative Zr anomaly, which is not observed in the CAT group. Fractionation of apatite and zircon during magmatic differentiation, and presence of Fe–Ti oxides among the fractionated liquidus phase (e.g., Foley and Wheller, 1990) may account for the negative breaks, whereas the presence of a crustal component in magma genesis (e.g., Taylor and McLennan, 1985) may respond for the positive anomalies.

Although the Tromaí Suite from the São Luís cratonic fragment also have features of high Sr–Ba association (Fig. 6A), other major and trace element relationships show differences in relation to the suite in the Gurupi Belt, with the latter showing some features akin to those of sanukitoids (Fig. 6B and C). The observed variations indicate differences in the magmatic evolution within the Tromaí Intrusive Suite. These variations are not easily explained by fractional crystallization as it was done for the well-characterized Tromaí Suite in the northern portion of the São Luís cratonic fragment (Klein et al., 2008). The absence of xenoliths in the studied suite suggests that assimilation of host rocks was not a determinant process in magma genesis. Probably, the major process was magmatic differentiation, which can occur via fractional crystallization and/or variable degrees of partial melting. As a whole, the chemical composition of the studied samples indicates a high Ba–Sr signature and a subduction-related tectonic setting for the Tromaí Intrusive Suite (Fig. 4E and F), with magmas derived from infracrustal sources.

#### 4.2.2. Canoa quartz diorite: petrography and geochemistry

Rocks from the western portion of the Tromaí composite batholith show distinctly different geophysical behavior from those of the eastern portion, with characteristic low radiometric values in the ternary RGB image (figure not included), and are hereafter termed Canoa quartz diorite. The rocks in this sector are hornblende-bearing quartz diorite and tonalite, with associated gabbro. This unit is composed of medium- to coarse-grained rocks (Fig. 3E), with preserved igneous textures (such as zoned plagioclase), but with evidence of low-grade metamorphism and/or widespread hydrothermal alteration. Tectonic features vary from slightly oriented plagioclase grains to penetrative foliation. The mineralogy comprises plagioclase (47%–73%), hornblende (5%–40%), and quartz (5%–25%). Titanite (≤2%) is ubiquitous, and ilmenite and opaque minerals are common. Zircon, apatite, and allanite are accessory phases.

The Canoa quartz diorite is metaluminous, but shows calcic and ferroan (tholeiitic) geochemical affinities (Fig. 4), in addition to low Sr/Y (≤11) and $(La/Yb)_n$ (~3) ratios, and very low $K_2O/Na_2O$ (<1) ratios, which consistently differ from the signature described above for the Tromaí Suite. The REE distribution is characterized by small fractionation of light from heavy elements, nearly flat HREE pattern, and moderately negative Eu anomalies (Fig. 5G), given by Eu/Eu* ratios of 0.6–0.7. The average HREE content is 143 ppm. LILE and HFSE are enriched in relation to the primitive mantle values (Fig. 5H), and only moderate fractionation is observed between the two sets of trace elements, which also present moderate breaks in the Nb, P, Zr, and Ti distribution. These breaks indicate fractionation of apatite and presence of Fe–Ti oxides among the fractionated liquidus phases, whereas the Nb

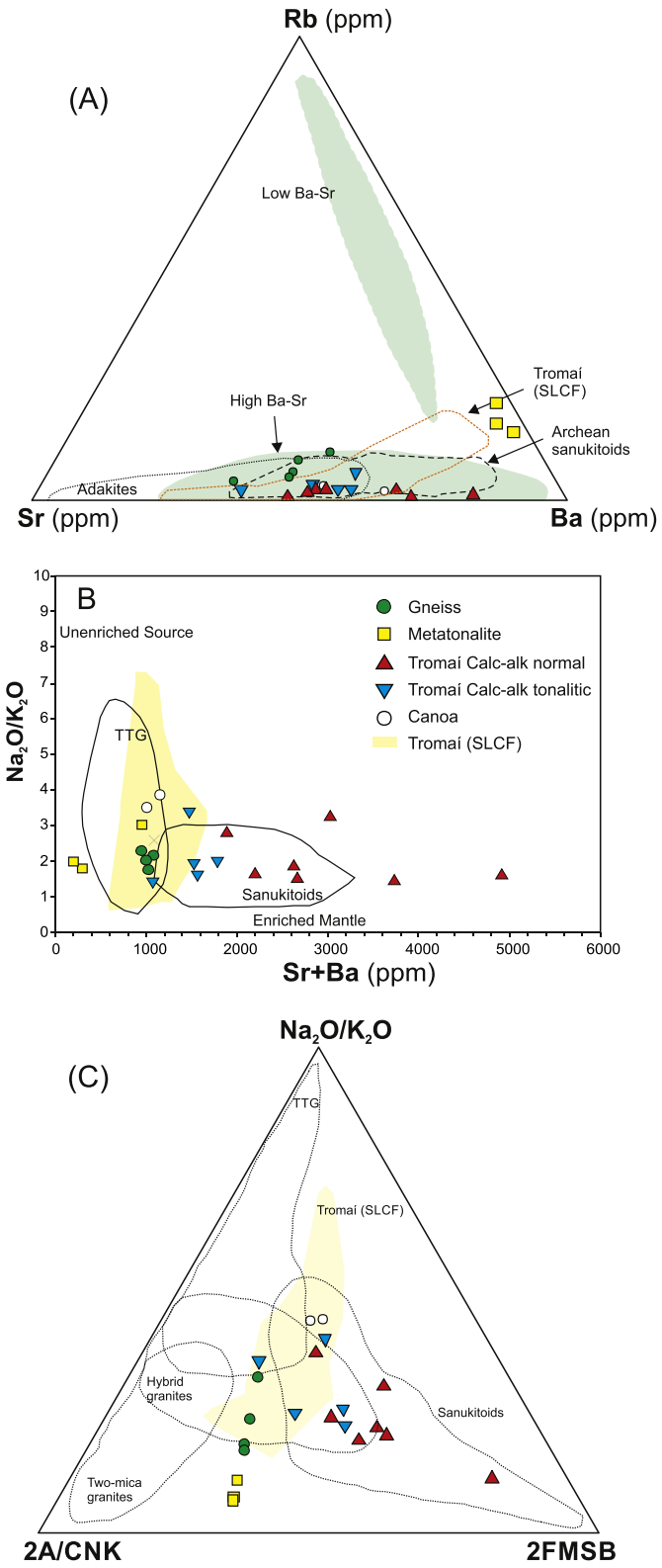


**Fig. 6.** (A) Discrimination diagram for high Ba–Sr granitoids with fields defined by Tarney and Jones (1994) and Peng et al. (2013). (B) Sr + Ba vs. $Na_2O/K_2O$ diagram (Halla et al., 2009). (C) Ternary classification diagram from Laurent et al. (2014). Triangle vertices are: 2*A/CNK (=$Al_2O_3$/(CaO + $K_2O$ + $Na_2O$) molar ratio); $Na_2O/K_2O$ and 2*FMSB [=($FeO^t$ + MgO) + (Sr + Ba) wt.%]. The field for granitoids of the Tromaí Suite in the São Luís cratonic fragment SLCF is presented for comparison (data from Klein et al., 2008).

anomaly is reflecting crustal input or fractionation of Nb-rich mineral(s), which is similar to what is observed in the Tromaí Intrusive Suite. The negative Zr anomaly probably reflects zircon fractionation. Positive yttrium anomaly, with enrichment of ten times the primitive mantle values, and relatively high Ga concentrations (Appendix D) are also remarkable characteristics. As such, the Canoa quartz diorite has not formed from the differentiation of basaltic melts or from internal or late fractionation (as interpreted for the Tromaí Suite – Klein et al., 2008), but from partial melting of an older basaltic protolith under relatively low-pressure conditions. Alternatively, crustal melting or incorporation of large amounts of crustal melts could account for the chemical features coming from the parental magma, and not reflecting the tectonic setting, which might be corroborated by the Archean $T_{DM}$ model age and the inherited zircon ages. Considering the association with the Tromaí Suite and the position in the batholith, the first hypothesis seems to be more likely.

### 4.3. Rhyacian amphibolites

#### 4.3.1. Field and petrographic characteristics

Small amphibolite bodies were included by Klein and Lopes (2011) in the Muriá and Cocal units, which crop out, respectively, within the domains of the Canoa quartz diorite and Vila Cristal Formation (Fig. 2). No clear contact relationships with the surrounding units could be determined. Both amphibolite units show the same $D_1$–$S_1$ foliation defined by the alternation of mafic and quartzo-feldspathic layers that we described for the gneisses of the Itapeva Complex.

Muriá comprises fine- to medium-grained rocks that are foliated to banded (Fig. 3F), granoblastic, and composed of plagioclase (35%–60%), hornblende (55%–60%), quartz (10%), and traces of opaque minerals. Epidote replaces hornblende. The protolith of the amphibolite was likely a gabbro or diorite that underwent metamorphism to the epidote-amphibolite or amphibolite facies and then retrogression (hydration) to form epidote.

The Cocal rocks are medium-grained (Fig. 3G) and show a N–S-trending $S_1$ banding that dips 70° to the east and that is locally folded. Amphibolite, epidote-amphibolite, and pyroxene-plagioclase-hornblende schists are the recognized petrographic types. These are composed of plagioclase (25%–38%), hornblende (45%–50%), clinopyroxene (≤15%), quartz (≤5%), titanite (3%–7%), and traces of opaque minerals and K-feldspar. The protoliths were probably basic plutonic rocks (gabbro) that underwent amphibolite to upper amphibolite (pyroxene-bearing types) metamorphism, i.e., slightly higher conditions than those presented by the Muriá amphibolite.

#### 4.3.2. Geochemistry

Compositionally the Muriá amphibolite is equivalent to basalts of the calc-alkaline series, whilst the Cocal amphibolite resembles tholeiitic basalts (Fig. 7). Muriá shows higher $SiO_2$ and Co, and lower $Al_2O_3$, CaO, $TiO_2$, Cr and Ni concentrations in relation to Cocal (Appendix D). Both types show flat REE distribution (Fig. 8A) with $(La/Yb)_n$ = 0.94–1.53, and enrichment of about ten times the chondritic values. This pattern indicates the absence of garnet in the residue after a high degree of partial melting of a relatively shallow mantle source, possibly of the MORB type (Wilson, 1989; Winter 2001). Muriá shows weak enrichment of LILE and depletion in HFSE when compared to MORB values (Fig. 8B). Weak negative Ta–Nb and Ti anomalies indicate the minor presence of residual phases, such as rutile, ilmenite or titanite in the mantle source, possibly reflecting a pre-subduction chemical component (Pearce, 1982; Condie, 1987; Wilson, 1989). In the Cocal amphibolite, the LILE distribution indicates elemental mobility, probably due to alteration and/or metamorphism. Deeply negative Ta–Nb, Zr–Hf, and Y anomalies and slightly positive Ce–P, and Sm–Ti anomalies distinguish Cocal from Muriá (Fig. 8B), in addition to lower Zr/Nb and Zr/Ta ratios for Cocal. These differences might indicate different petrogenetic processes involved in the genesis of the two amphibolite types, including the

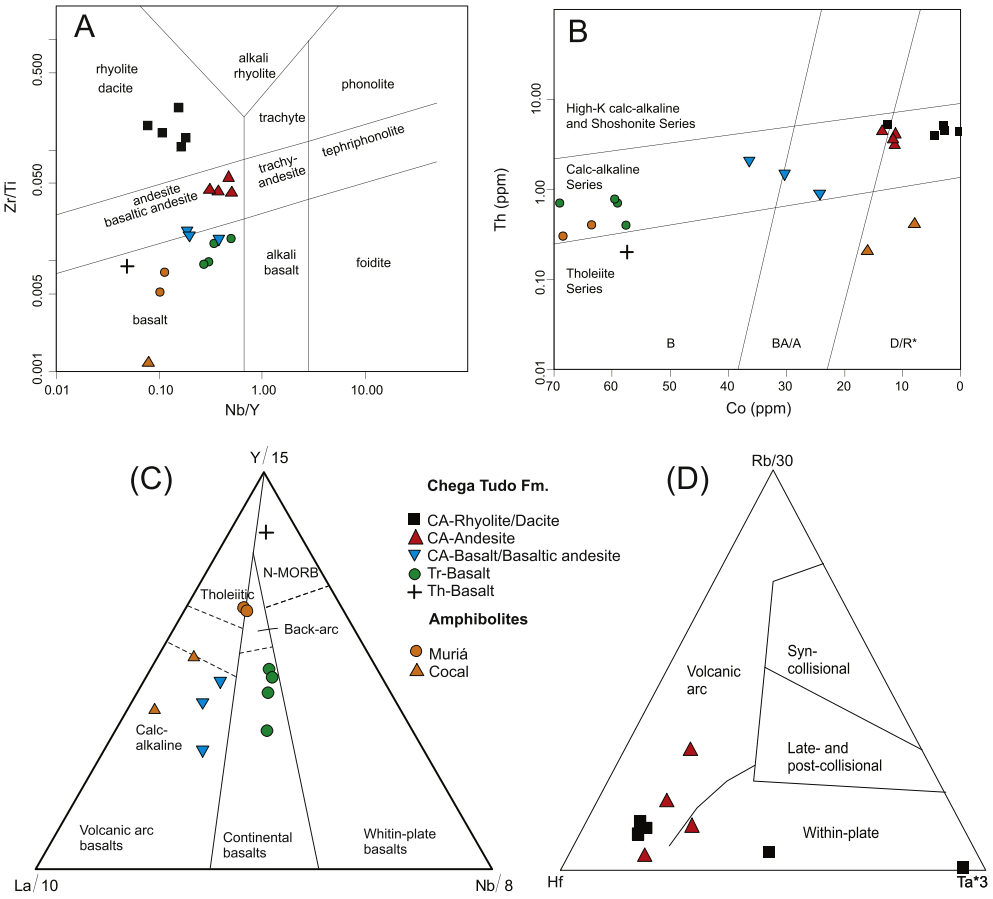


**Fig. 7.** Chemical classification of volcanic rocks. The Rhyacian amphibolites are included for comparison. (A) According to Winchester and Floyd (1977) modified by Pearce (1996), and (B) according to Hastie et al. (2007). Tectonic discrimination diagrams for Rhyacian amphibolites and volcanic-metavolcanic rocks. (C) According to Cabanis and Lecolle (1989) for basic rocks. (D) According to Harris et al. (1986) for acidic to intermediate rocks. Magmatic series abbreviations: CA: calc-alkaline, Tr: transitional, Th: tholeiitic.

degree of crust contamination, and/or different tectonic setting for the magmas, along with element transportation by partial melts (Cocal) or by fluids (Muriá) (e.g., Hawkeswork and Powell, 1980). The Th/Nb ratios above 0.2 for Cocal strongly suggest contamination.

The calc-alkaline affinity associated with flat REE distribution, the relatively high $La_n/Sm_n$, Zr/Nb, and Zr/Ta ratios, in addition to the spatial (Fig. 2) and temporal (see geochronology section) association with the Tromaí-Canoa granitoids are consistently suggestive of an orogenic setting (island arc?) for Muriá. A similar tectonic setting is suggested for Cocal (Fig. 7C), but with petrogenetic/contamination differences, as stated above.

### 4.4. Rhyacian volcanic and metavolcanic rocks

#### 4.4.1. Field and petrographic characteristics

The Rhyacian volcanic and metavolcanic rocks are part of the volcano-sedimentary Chega Tudo Formation, which forms an elongated to arcuate, NW–SE to N–S trending sequence that crops out near the boundary between the Gurupi Belt and the São Luís cratonic fragment (Fig. 2). The magmatic lithological content of the formation comprises rhyolite, dacite, andesite, basalt, chlorite schist, muscovite schist, hornblende schist, talc schist and tremolite schist (Bettencourt et al., 1991; Ribeiro, 2002; Yamaguti and Villas, 2003; Klein et al., 2005a, 2015; Klein and Lopes, 2011), i.e., felsic, intermediate, mafic and ultramafic components. Some volcanic varieties are metamorphosed and deformed, others are preserved (Fig. 3H and I). These volcanic and metavolcanic rocks occur predominantly interleaved in sedimentary (phyllites and pelitic schists, carbonaceous or not) and volcanoclastic layers (volcanogenic sandstones), but also form individual, mappable bodies.

Rhyolites, dacites, and andesites are porphyritic rocks exhibiting quartz (12%–30%) and/or plagioclase (30%–70%) phenocrysts, locally showing embayment produced by magmatic corrosion. The matrix is quartzo-feldspathic, with minor amounts of white mica, biotite, and chlorite. Hornblende and actinolite occur only occasionally, whereas ilmenite, rutile, apatite, epidote, and magnetite are accessory phases. The mafic types (schists) present variable proportions of hornblende (up to 70%–75% in hornblende schists), chlorite, plagioclase, epidote, calcite, opaque minerals and quartz, whilst ultramafic varieties are composed of tremolite, actinolite, talc, chlorite, and calcite. Metamorphic conditions vary from lower greenschist to the greenschist-amphibolite transition (450 °C, 2–3 kbar; Pastana, 1995; Yamaguti and Villas, 2003).

The age of volcanism was established at 2148 ± 1 to 2160 ± 3 Ma (Klein and Moura, 2001; Pb evaporation in zircon), and Nd model ages range from 2.20 to 2.28 Ga, with $\varepsilon_{Nd}(t)$ of +1.1 to +2.7 (Klein et al., 2005a), which indicates juvenile sources for the parental magmas.

#### 4.4.2. Geochemistry

The geochemical results (Appendix D) show that some of the samples have moderate to high LOI and total carbon percentages, indicating alteration. As such, this discussion is based mostly in relatively immobile minor and trace elements (e.g., Pearce, 1996; Hastie et al., 2007), although major elements such as $SiO_2$, FeO, $Na_2O$ and the Nb/La ratio do not show covariance with LOI (figure not included), suggesting absence of significant mobility. Furthermore, with one exception, the Ce/Ce* values (0.90–1.08) indicate lack of REE mobility (e.g., Polat et al., 2002).

Based on the chemical classifications of volcanic rocks (Winchester and Floyd, 1977 modified by Pearce, 1996; Hastie et al., 2007), and on the REE distribution, five groups of volcanic rocks can be considered (Figs. 7 and 8): (1) calc-alkaline rhyolite/dacite, (2) calc-alkaline andesite/basaltic andesite, (3) calc-alkaline basaltic andesite to basalt, (4) transitional basalt, and (5) tholeiitic basalt. The three calc-alkaline types show trace-element characteristics of volcanic to continental arc rocks,

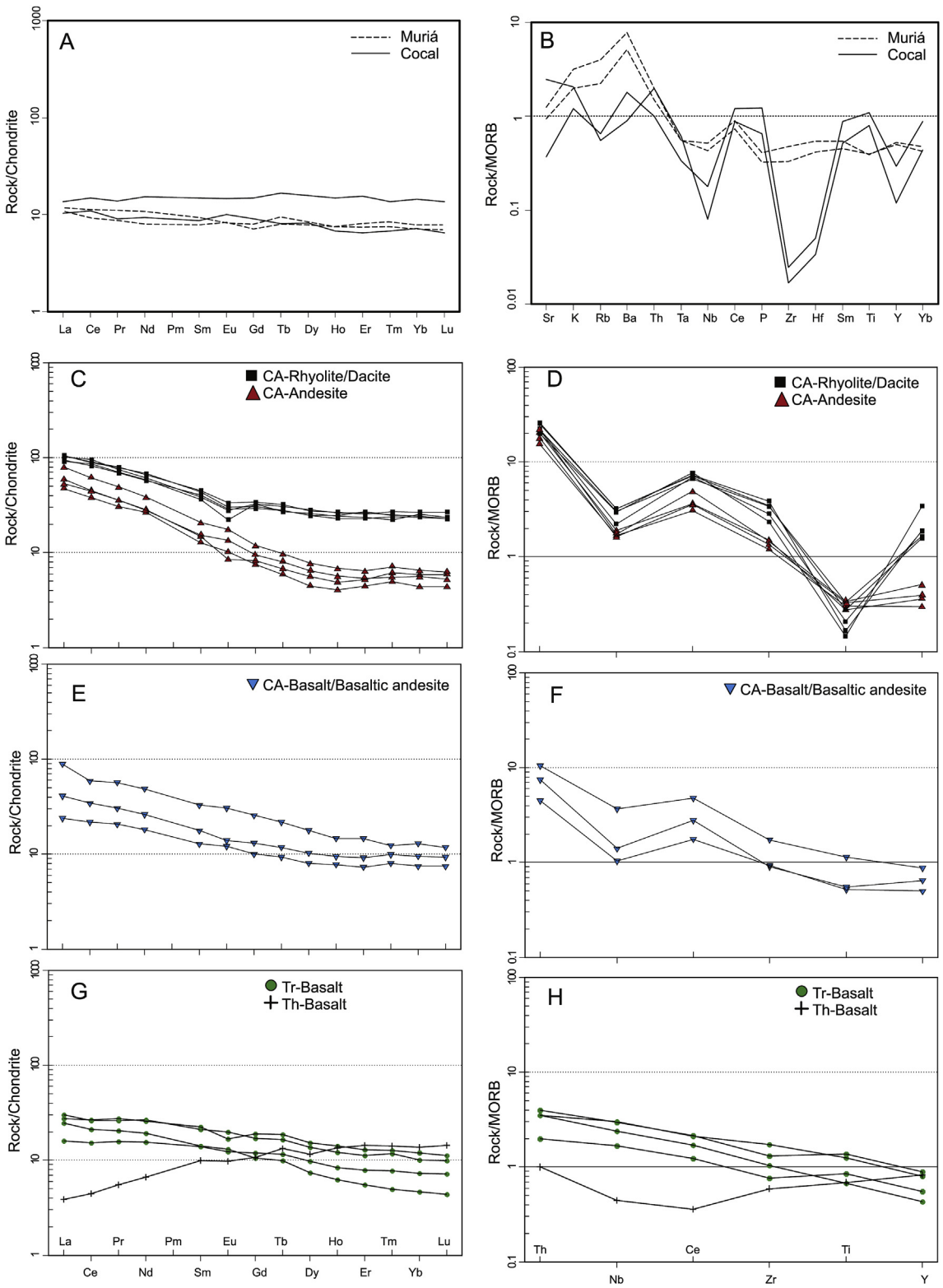


**Fig. 8.** (A, C, E and G) Chondrite-normalized REE and (B, D, F and H) MORB-normalized trace elements distribution for the Rhyacian amphibolites (Muriá and Cocal), and Rhyacian volcanic and metavolcanic rocks (Chega Tudo Formation). Normalization according to Boynton (1984) and Sun and McDonough (1989), respectively. Magmatic series abbreviations: CA: calc-alkaline, Tr: transitional, Th: tholeiitic.

such as the negative Nb anomaly relative to Th and Ce, whereas basalts have transitional to marginal basin and continental characteristics (Figs. 7 and 8). All basalts have Th/Nb ratios greater than 0.2, indicating crustal contamination (Pearce, 2008).

### 4.5. Peraluminous magmatism

Several bodies of biotite- and muscovite-bearing granites crop out along the entire Gurupi Belt forming an NW–SE corridor (Fig. 2). Many of these granites have already been characterized in terms of petrography,

geochemistry, Nd composition, and U–Pb geochronology. Three different intrusion episodes have been defined to date, occurring at 2142 ± 9 Ma, 2100 ± 15 Ma (Klein et al., 2012), and 549 ± 4 Ma (Palheta et al., 2009).

A number of additional bodies of two-mica granites were mapped in this work (Fig. 2 – plutons without geochronological information). These granites are leucocratic monzogranites and syenogranites (Fig. 3J), in general foliated, and locally banded. At least one of these bodies show to be intrusive in mica schist of the Paleoproterozoic Santa Luzia do Pará Formation (dikes and apophyses intruding schists). We have also found another pluton to the west of the Gurupi belt, within the Phanerozoic cover, cropping out near the occurrence areas of the Rhyacian Jonasa and of the Neoproterozoic Ney Peixoto granites (Fig. 2B). This granite, named Pantoja, is a slightly foliated to banded granodiorite (Fig. 3K) composed of quartz (25%), plagioclase (30%), microcline (10%), muscovite (20%), and biotite (5%).

#### 4.5.1. Rhyacian peraluminous granites

The dated Rhyacian peraluminous granites form two different groups. The youngest group (Japiim Suite, ~2100 Ma) comprises strongly peraluminous rocks, derived from melting of crustal protoliths, and consistent with collision-type magmatism (Klein et al., 2012). The oldest group (Jonasa Granite, ~2142 Ma) is only weakly peraluminous and has been interpreted as a late manifestation of continental arc potassic magmatism (Klein et al., 2012).

#### 4.5.2. Neoproterozoic peraluminous granite

Bodies of the biotite- and muscovite-bearing Ney Peixoto Granite occur to the west of the Gurupi Belt and crop out as small erosive windows within Phanerozoic sediments (Fig. 2B). The granite is only slightly foliated to banded and contains quartz (28%), plagioclase (14%), microcline (45%), muscovite (7%), biotite (5%), and apatite (1%). Villas and Sousa (2007) have also identified orthoclase (~6%), A/CKN ratio greater than 1.1, and estimated the crystallization conditions at 600–650 °C and 5 kbar. The granite presents a zircon age of 549 ± 4 Ma (Pb-evaporation), and Sm–Nd model age of 1.70 Ga, with the $\varepsilon_{Nd}$ value of −8 (Palheta et al., 2009), with initial $^{87}Sr/^{86}Sr$ of 0.704 (Villas, 1982).

### 4.6. Neoproterozoic peralkaline intrusion

In the west of the Gurupi Belt, a body of nepheline-syenite gneiss crops out within the Phanerozoic cover (Fig. 2B). This alkaline rock was dated at 732 ± 7 Ma (Klein et al., 2005a), and detailed petrographic and geochemical studies were reported by Villas (1982) and Lowell and Villas (1983). The intrusion is composed of nepheline, albite, perthite, plagioclase, biotite, and pyrochlore, with apatite, zircon, carbonate, sodalite, cancrinite, white mica and pyrite as accessory minerals (Villas, 1982). The rock is peralkaline to weakly metaluminous, and deformation and metamorphism under amphibolite-facies conditions produced gneissic banding and local migmatization (Lowell and Villas, 1983).

Villas (1982) have reported an initial $^{87}Sr/^{86}Sr$ of 0.7034, whereas a K–Ar age of 580 ± 10 Ma was determined on biotite, which might reflect metamorphism (Lowell and Villas, 1983; Klein et al., 2005a and references therein).

### 4.7. Neoproterozoic metamorphosed calc-alkaline intrusion

#### 4.7.1. Field and petrographic characteristics

Klein and Lopes (2011) identified small bodies of a fine-grained, greenish to greyish tonalite and subordinate quartz diorite (Caramujinho metamicrotonalite) that crop out in spatial association with the Muriá amphibolite and the Canoa quartz diorite (Fig. 2). The rocks are slightly foliated, locally banded (Fig. 3L), inequigranular to porphyritic in texture, with small plagioclase, hornblende, and quartz phenocrysts set in a matrix composed of plagioclase, quartz, epidote, sericite, amorphous titanite, and calcite. Zircon, allanite, titanite, and apatite are accessory phases. The metamorphic destabilization of hornblende produced actinolite, biotite, chlorite, and epidote, whereas plagioclase was replaced by epidote and sericite.

#### 4.7.2. Geochemistry

The Caramujinho metamicrotonalite is an intermediate, low- to medium-K, calc-alkaline, and metaluminous unit (Fig. 4). The REE concentrations are enriched in relation to the chondrite, and their distribution shows moderate fractionation between light and heavy elements [$(La/Yb)_n$ = 11–14], and incipient positive europium anomaly (Fig. 9A). The LIL and HFS elements are enriched in relation to the primitive mantle, fractionated, with weak to moderate Th, Pb, Zr, and Ti, and strong Nb negative anomalies, and positive Sr and Nd anomalies (Fig. 9B). This geochemical behavior is similar to those presented by the Paleoproterozoic Tromaí Suite, indicating subduction-related magma source and orogenic setting (Fig. 4). However, it is uncertain if this signature reflects the tectonic setting in which the Caramujinho unit formed or the tectonic setting of the magma source since the U–Pb zircon and whole-rock Sm–Nd data (see next sections) indicate crustal origin for the parental magmas.

## 5. U–Pb geochronology

Zircon crystals from plutonic and metaplutonic rocks were dated by the U–Pb SHRIMP and LA-ICP-MS techniques. Sampling locations are shown in Fig. 2, the geographic coordinates are listed in Appendices A and E and the analytical results are shown in Appendix E. Zircon/spot analyses used for age calculation, inherited zircons, and discarded analyses (in general by high common Pb and/or high analytical errors) are specified in the tables from Appendix E. The ages quoted in this section, except where stated differently, are $^{207}Pb/^{206}Pb$ apparent ages (e.g. Spencer et al., 2016). Cathodoluminescence and/or backscattering electron images of zircon and titanite grains are presented in Fig. 10, whereas concordia plots used to demonstrate the age calculations are shown in Fig. 11. Additional concordia (Wetherhill and/or Tera-Wasserburg) and weighted mean ages are also presented in Appendix F.

### 5.1. Rhyacian gneiss-metatonalite complex (Itapeva Complex)

Sample EK163A (LA-ICP-MS) is a biotite-quartz-feldspar gneiss sampled in a small isolated body northwest of the main massif of the Itapeva Complex (Fig. 2). The zircon of this sample is prismatic, about 200 μm long, with inclusions and fractures. In BSE image discrete oscillatory zonation is observed (Fig. 10). The isotopic ratios obtained from twenty-four spot analyses performed on twenty-three crystals (one discarded due to high analytical error) yielded two groups of $^{207}Pb/^{206}Pb$ apparent ages. Two spots on a single grain show slightly discordant Archean ages (2.7 Ga), but most of the crystals have apparent ages between 2.13 and 2.18 Ga (Fig. 11A). Although relatively aligned, data with large discordance also show large dispersion of the $^{207}Pb/^{206}Pb$ apparent ages. Perhaps this behavior is a consequence of some disturbance, or the analysis might have incorporated tiny unobserved inclusions. Therefore, using ten concordant crystals (<2% of discordance, Appendix E), a concordia age of 2148 ± 4 Ma is obtained (Fig. 11A). This age is interpreted as the crystallization age of the igneous protolith of the gneiss. The Archean age is considered as inheritance, or, alternatively, it may represent crustal contamination (no core observed in images).

Sample EK311A (SHRIMP) is a garnet-bearing biotite-metatonalite occurring in the central portion of the main massif of the complex. Most of the analyzed zircons are idiomorphic to subidiomorphic and show magmatic oscillatory zoning (Fig. 10). Some crystals show sector zoning. Twenty-four analyses were carried out on nineteen crystals (one rim), and the regression through all data yielded upper and lower intercept ages at 2154 ± 11 Ma and 447 ± 130 Ma, respectively (MSWD = 2.7) (Fig. 11B). The isotopic ratios of zircon 10.1-R measured in low luminescent rim of the crystal is highly discordant, with high U contents, and

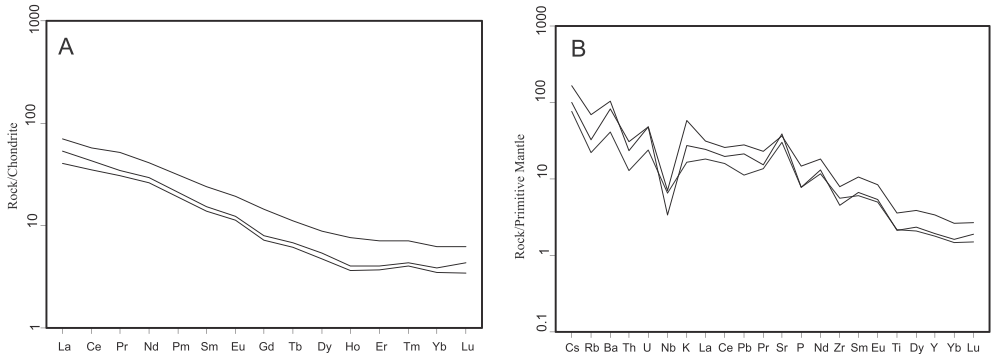


**Fig. 9.** (A) Rare earth elements and (B) primitive mantle-normalized trace element distribution for samples of the Neoproterozoic calc-alkaline intrusion. Normalization according to Boynton (1984) and Sun and McDonough (1989), respectively.

can be discarded from the calculation. The remaining analyses show $^{207}Pb/^{206}Pb$ apparent ages ranging from 2115 ± 37 to 2171 ± 15 Ma, whereas the isotopic ratios of zircon 20 plot on the concordia curve defining an age of 2208 ± 9 Ma, which is better interpreted as inheritance. The regression through the remaining 22 spot analyses defined upper and lower intercept ages of 2149 ± 8 Ma, and 230 ± 120 Ma (MSWD = 1.14), respectively, which define the crystallization age of the tonalite, and younger lead loss.

### 5.2. Rhyacian calc-alkaline high Ba–Sr and ferroan granitoids

Sample EK187A (LA-ICP-MS) is a foliated biotite-granodiorite attributed to the Tromaí Intrusive Suite (high Ba–Sr, calc-alkaline tonalitic magmatic series). The zircon crystals are euhedral to subhedral and show variable morphologies: mono-pyramidal, asymmetric pyramids, few prismatic and ellipsoidal. All crystals show oscillatory zoning and many have thin, highly luminescent external rims indicating localized metamictization. Few crystals show evidence of resorption or modification of the oscillatory zoning to a structureless and low-luminescent layer (Fig. 10). Twenty-six spot analyses were carried out on twenty-four crystals, and the whole dataset shows Th/U ratios that are consistent with magmatic values (>0.13). The data of nine core analyses were discarded due to their high analytical errors in the $^{206}Pb/^{238}U$ apparent ages (greater than 5%). The isotopic ratios of the remaining seventeen concordant spots (discordance <4%) located in zircon cores and rims returned an age of 2174 ± 5 Ma (MSWD = 0.17, Fig. 11C), which is interpreted as the crystallization age of the granodiorite.

Sample EK37 (LA-ICP-MS) is a coarse-grained metatonalite from the ferroan Canoa quartz diorite unit. Twenty-seven spot analyses were performed on twenty-three crystals and all analyses returned Th/U ratios above 0.11 (magmatic zircons). Two zircon morphological populations can be observed (Fig. 10), which form parallel arrays in the concordia plot (Fig. 11D). (1) Predominantly ellipsoidal crystals that frequently show sector zoning with moderate to high luminescence define one group. These crystals show, in general, slightly higher isotopic ratios than the other group and, in consequence, rather higher $^{207}Pb/^{206}Pb$ apparent ages, ranging from 2169 ± 24 to 2214 Ma. The regression through fourteen spot analyses (MSWD = 0.55) yielded an upper intercept age of 2192 ± 10 Ma. (2) The other group comprises predominantly pyramidal and prismatic crystals with fine oscillatory zoning. The isotopic ratios of ten rim and core analyses align along a regression line that intercepts the concordia curve at 2162 ± 11 Ma (MSWD = 0.84). The age of the second group is interpreted as the crystallization age of the tonalite. The older ages of the first group represent inheritance. The discordia lines of the two groups yielded lower intercepts ages with large analytical errors at 533 ± 370 Ma and 596 ± 100 Ma. Notwithstanding, these ages indicate Pb loss during a Neoproterozoic-Cambrian event. Among the discarded analyses, two zircons (Z13 and Z33) yielded younger concordant ages at 2102 and 2025 Ma, which were discarded because their isotopic ratios are different from those of the two groups described above. One of the crystals is fractured and the other one shows irregular internal structure. It is possible that the U–Th–Pb system behaved open for these crystals, but the cause of this behavior is uncertain. The age of 2102 Ma is well represented by the peraluminous magmatism in the Gurupi Belt (Klein et al., 2012 and this study), whereas an age of close to 2025 Ma was only found in a distant small igneous body in the São Luís cratonic fragment (2011 Ma, Klein et al., 2014). Orogenic gold mineralization and metamorphism are also associated with these younger ages. Therefore, fluids from the peraluminous magmatic events or metamorphic-hydrothermal fluids associated with gold mineralization could have caused lead loss associated with partial resorption and reprecipitation of the zircon crystals. Such a situation has been described for an undeformed volcanic sequence of the Kaapvaal Craton of Southern Africa (Poujol et al., 2005), but the cause of the concordance remains enigmatic.

### 5.3. Rhyacian amphibolites (Muriá and Cocal)

Sample EK31 (SHRIMP) is a foliated amphibolite of the Muriá unit. Zircon crystals show typical igneous sector and concentric oscillatory zoning, euhedral to anhedral morphologies, and some consist of fragments. Some crystals show overgrowths and/or structureless rims truncating the igneous zoning (Fig. 10). Isotopic results were obtained in fifteen spots on nine crystals. All crystals show Th/U ratios within the magmatic field (>0.27), discordance (some reverse) between 2% and 37%, and core and rim ages are rather similar within uncertainties. Crystals 2 and 10 show distinctly low luminescence, relatively higher Th contents, and younger $^{207}Pb/^{206}Pb$ apparent ages (Fig. 11E, Appendix E). Discarding the data from crystal 2 (core and rim) and crystal 10 (rim), a statistically coherent group of twelve analytical points yield an intercept age of 2136 ± 19 Ma (MSWD = 3.0) (Fig. 11E), which defines the minimum crystallization age of the igneous protolith of the Muriá amphibolite. The maximum crystallization age is taken from the nearly concordant zircon 10.1 at 2179 ± 18 Ma. This age overlaps within uncertainties with the age of the Cocal amphibolite (see below) and may be the best approximation of the crystallization age.

For the Cocal unit, one titanite and two zircon samples from two different amphibolite bodies (Fig. 2) were dated by the LA-ICP-MS technique. All crystals show Th/U ratios compatible with those of the magmatic field. Only twelve zircon crystals were recovered from sample EL122A, and fourteen spot analyses were performed. Backscattering electron images show prismatic and fragments of crystals with oscillatory to diffuse zoning (Fig. 10). One zircon (Z02) was discarded due to high common Pb content, and crystal Z06 indicates an Archean source of 2586 ± 11 Ma, interpreted as crustal contamination. Nine variably discordant spot analyses, including cores and rims, plot along a discordia line that intercepts the concordia at 2162 ± 8 Ma (MSWD = 1.3, Fig. 11F) and ancient/episodic Pb loss is suggested by the Tera-Wasserburg plot (Appendix F). This age may be interpreted as the crystallization age of the

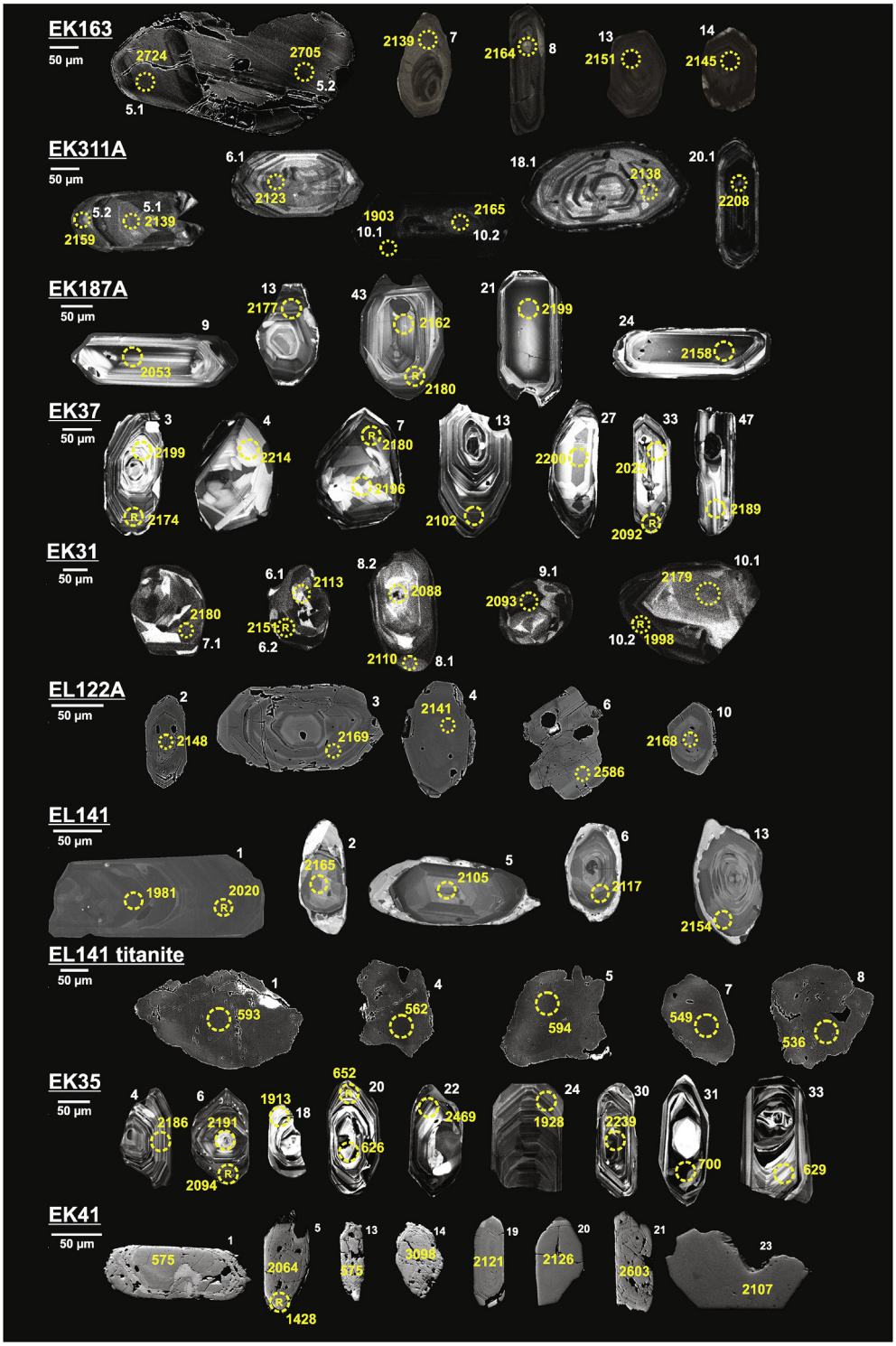


**Fig. 10.** Cathodoluminescence and Backscattering Electron images of representative zircon crystals (and one titanite sample). White numbers refer to the zircon/titanite numbers in data tables from Appendix E. Yellow numbers stand for the apparent ages ($^{207}Pb/^{206}Pb$ for samples older than 1000 Ma, $^{206}Pb/^{238}U$ for samples younger than 1000 Ma).

igneous protolith of the sample. Three crystals that do not align along this discordia, and have higher $^{207}Pb/^{206}Pb$ apparent ages around 2.25 Ga. These are also interpreted as inheritance.

Zircon crystals from sample EL141 show rounded to irregular/corroded rims, and are mostly structureless or with diffuse zoning (Fig. 10). Twenty spot analyses were carried out on eighteen crystals. One crystal with $^{207}Pb/^{206}Pb$ apparent age of 2677 ± 29 Ma shows high common Pb content and was discarded. Two analyses (core and rim) in crystal Z01 show isotopic ratios that are not coherent with those of the predominant group of zircons and were also discarded. This behavior may have a similar explanation to that provided to the Rhyacian metatonalite (EK37) in the previous section. The regression of the remaining seventeen spot analyses on sixteen crystals produced a discordia line (MSWD = 0.55) that defines upper and lower intercept ages of 2166 ±

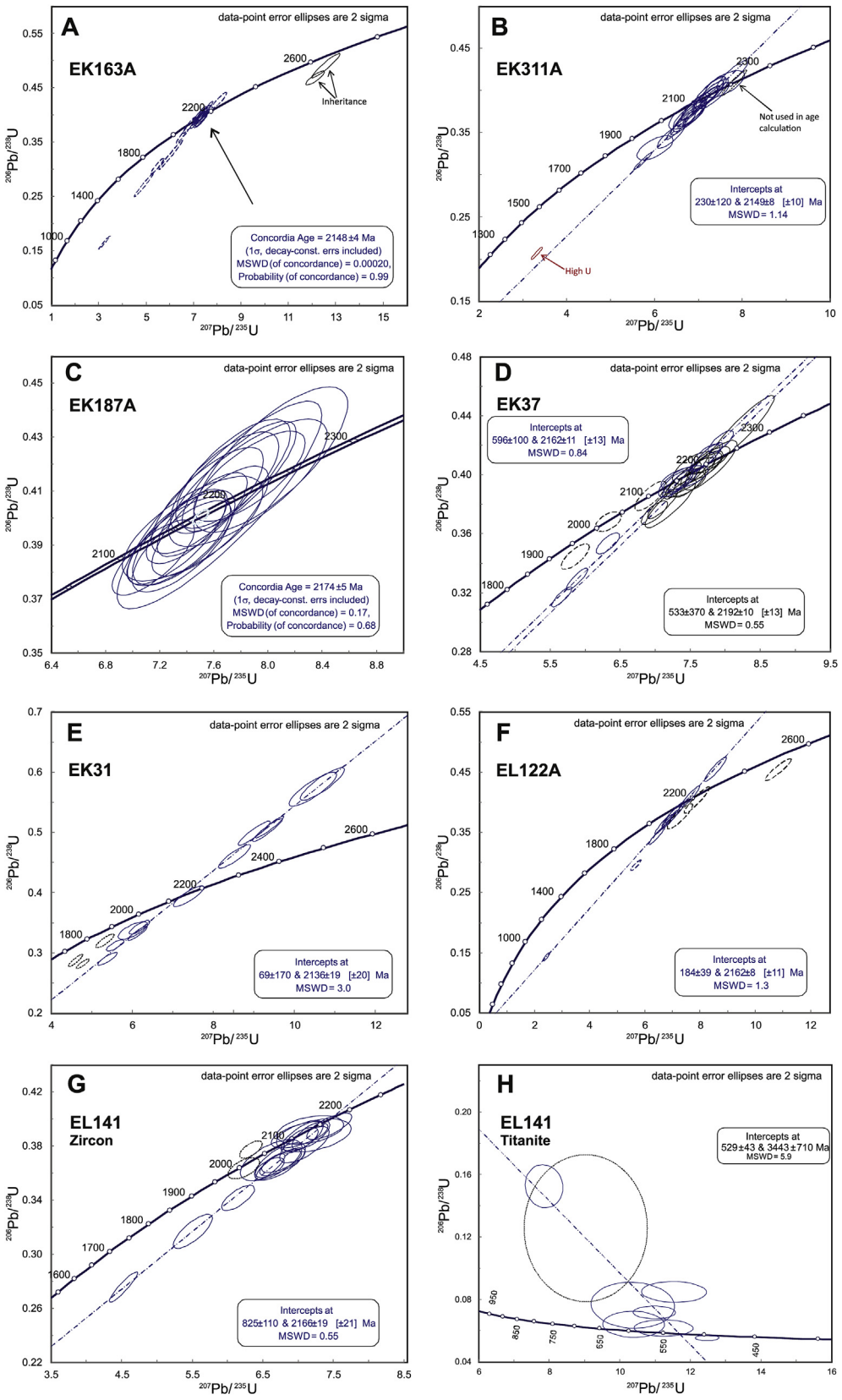


**Fig. 11.** Concordia diagrams for gneiss, granitoids, and amphibolite units. Additional diagrams are available in Appendix F (Electronic Supplementary Data). (A) Gneiss (EK163A) and (B) metatonalite (EK311A) samples of the Rhyacian complex. (C) Granodiorite (EK187A) of the Rhyacian high Sr–Ba suite. (D) Tonalite (EK37) of the Rhyacian ferroan granitoid. (E) Muriá amphibolite (EK31). (F) Cocal amphibolite (EL122A). (G) Zircon and (H) titanite of the Cocal amphibolite (EL141). (I) Rhyacian peraluminous suite EL78B. (J, K and L) Neoproterozoic calc-alkaline intrusion (EK35). (M, N) Neoproterozoic peraluminous granite (EK41).

19 Ma and 825 ± 110 Ma, respectively (Fig. 11G). The younger age might indicate Pb loss due to a Neoproterozoic event. The older age overlaps within analytical uncertainties the age found in sample EL122A of the same amphibolite unit and that is interpreted as the crystallization age of the igneous protolith of the amphibolite.

Eight titanite grains were recovered from sample EL141. The grains

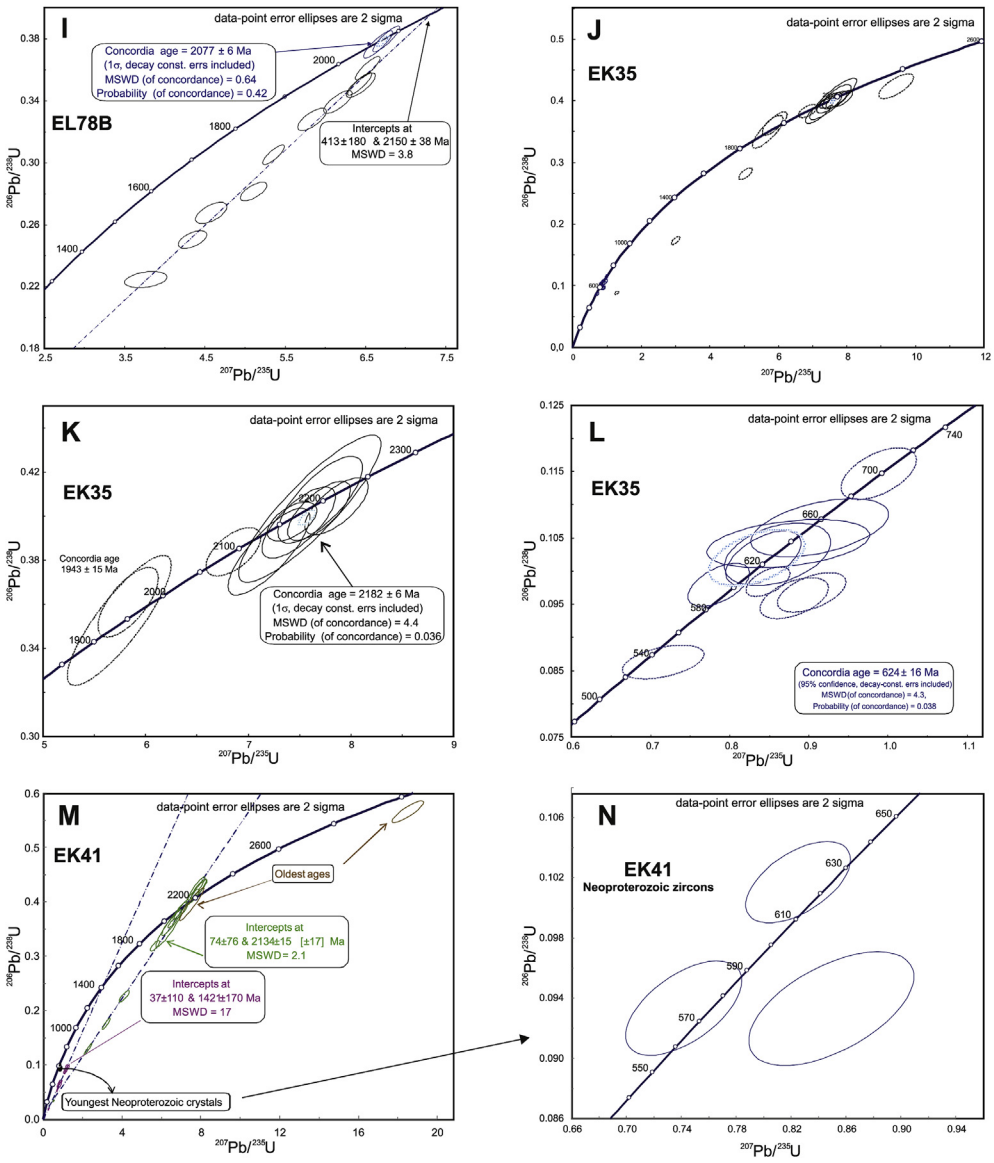


**Fig. 11.** (*continued*).

are brown, euhedral to subhedral, and rich in mineral inclusions (Fig. 10 and Appendix C). The analytical results show spread in the isotopic ratios, variable discordance (2.5%–41.6%), $^{206}Pb/^{238}U$ apparent ages between 497 ± 5 and 773 ± 25 Ma, and lack of good alignment of the whole set of analyses. Discarding only the analysis with a huge error (tit-3), the regression through the remaining spots indicates an age of 529 ± 43 Ma (MSWD = 5.9), and an upper intercept with very large error and unrealistic old age (Fig. 11H). Considering the zircon age pattern in the Cocal amphibolite samples, the titanite ages have likely been produced by a thermal event (metamorphism) a long time after crystallization.

### 5.4. Paleoproterozoic peraluminous granites

Sample EL78B (SHRIMP) is a biotite-muscovite monzogranite from a stock of "undifferentiated granitoids" mapped by Klein et al. (2015) (Fig. 2). Zircons are mostly elongated and prismatic, with oscillatory zoning. Some have thin, irregular to spongy rims. Fourteen analytical spots were obtained on thirteen zircon crystals (Appendix E), with $^{207}Pb/^{206}Pb$ apparent ages ranging from 1666 to 2302 Ma. Two analyses were discarded due to high uranium or common Pb contents. Two crystals (4.1 and 15.1) are concordant and define a concordia age of 2077 ± 6 Ma (MSWD = 0.64) (Fig. 11I). Ten variably discordant analyses (on nine crystals) allowed to draw a discordia line with reasonable fit (MSWD = 3.8). The upper and lower intercepts of this discordia indicate ages of 2150 ± 38 Ma and 413 ± 180 Ma, respectively (Fig. 11I). This age pattern repeats what was described by Klein et al. (2012) for the Paleoproterozoic strongly peraluminous granites of the Gurupi Belt, i.e., crystallization age between ca. 2070 and 2120 Ma, and older Paleoproterozoic inheritance (ca. 2140–2170 Ma). Therefore, the concordant age of 2077 ± 6 Ma is interpreted as the crystallization age of the granite, and allows us to relate it to the peraluminous Japiim Suite (Fig. 2). The upper and lower intercept ages represent respectively inheritance and possible lead loss in the Neoproterozoic–Cambrian.

### 5.5. Neoproterozoic calc-alkaline intrusion (Caramujinho metamicrotonalite)

Results were obtained in 24 spot analyses (LA-ICP-MS) in eighteen zircon crystals from sample EK35. Cathodoluminescence images (Fig. 10) and isotopic ratios (Fig. 11J) indicate several zircon populations, with $^{207}Pb/^{206}Pb$ and $^{206}Pb/^{238}U$ apparent ages in the range of 1913 ± 19 Ma to 2469 ± 18 Ma and 534 ± 6 Ma to 700 ± 9 Ma, respectively. A group of relatively small (0.12–0.15 mm), euhedral to subhedral, sometimes fragmented crystals, shows well-defined oscillatory zoning (Fig. 10), and

has Paleoproterozoic apparent ages (11 crystals, 13 spots). Seven crystals from this group are concordant and define an age of 2182 ± 6 Ma (Fig. 11K, Appendix E). The Th/U ratios of this group range from 0.20 to 0.63 and are consistent with the magmatic field. With morphologic characteristics and Th/U ratios that are similar to this group, crystals 18 and 24, with discordance lower than 2%, show different isotopic ratios and define a concordant age of 1943 ± 15 Ma (Fig. 11K). The population with Neoproterozoic apparent ages, is formed mostly by euhedral (some fragmented) and prismatic crystals that also show oscillatory zoning, but with some differences in the internal structure of cores and rims, especially variation in the luminescence (Fig. 10). The Th/U ratios range from 0.19 to 0.41 and moderate to discordant analyses and those with high Pb concentration were not used in age calculations. The isotopic ratios of four crystals from this group (four cores and one rim) define a concordant age of 624 ± 16 Ma (Fig. 11L). If eight Neoproterozoic crystals are considered, a weighted mean age of 611 ± 17 Ma (MSWD = 6.5) is obtained (Appendix F), being indistinguishable of the concordia age within uncertainties. Another concordant crystal (z31 in Appendix E) shows internal structure characterized by larger concentric zones, an apparently structureless (or modified) and highly luminescent core, and possibly, partial destruction of the zoning in the portion of the crystal that was affected by fractures. The isotopic ratios of this crystal define a concordant age of 699 ± 8 Ma. The data above suggest crystallization age of 624 ± 16 Ma for the microtonalite, and the age of 2182 ± 6 Ma is due to inheritance. The other two concordant ages might also represent inheritance or, alternatively, Pb loss associated with partial resorption and reprecipitation of the crystals during the crystallization of the host microtonalite.

### 5.6. Neoproterozoic peraluminous granite (Pantoja Granite)

Sample EK41 (LA-ICP-MS) is a biotite-muscovite bearing granodiorite of the Pantoja unit. At least two zircon populations are observed in BSE images (Fig. 10). Fractured crystals, with homogeneous cores and porous/spongy rims predominate. Locally, the rims are preserved from alteration. The subordinate population comprises fractured and more homogenous crystals, with no significant separation between core and rim. Thirty-one spot analyses in twenty crystals show Th/U ratios mostly in line with those of magmatic zircons and produced very variable isotopic ratios and degree of discordance. Four groups of ages were obtained from these isotopic ratios (Fig. 11M). Data of nine spots were discarded due to elevated common lead contents and/or analytical errors. The cores of the main morphologic type show Archean (two grains with ages of 2.6 and 3.1 Ga), and predominantly Paleoproterozoic $^{207}Pb/^{206}Pb$ apparent ages. The rim of the 2.6 Ga-old core yielded an apparent age of about 2.2 Ga. The regression of Paleoproterozoic data indicates upper and lower intercept ages of 2134 ± 15 Ma and 74 ± 76 Ma (MSWD = 2.1). The porous rims of the 2.1 Ga core population present very discordant isotopic ratios and $^{207}Pb/^{206}Pb$ apparent ages of 1.3–1.7 Ga and form a poorly-defined (MSWD = 17) regression line that intercepts the concordia curve at 1421 ± 170 Ma (Fig. 11M). Finally, two more homogeneous crystals (Z01 core and rim, Z13) show younger (Neoproterozoic) apparent ages (Fig. 11N). A regression line could not be obtained with the data, which yielded a weighted mean age of 595 ± 51 Ma (MSWD = 0.44) calculated from the individual $^{206}Pb/^{238}U$ apparent ages (Appendix F). This complex dataset does not allow a categorical definition of the crystallization age of the granite. However, we assume the Neoproterozoic weighted mean age, despite the large error, to be the best approximation of the crystallization age of the granite, whereas all the other older ages are inheritance (see more in the discussion section).

## 6. Sm–Nd whole-rock isotopic data

New Nd isotope data are listed in Table 1, and available data are compiled in Appendix A. Orthogneisses (biotite-gneiss) and the garnet-bearing biotite (and/or epidote-biotite) metatonalite included in the Itapeva Complex (Rhyacian gneiss-metatonalite complex) show similar $^{147}Sm/^{144}Nd$ (~0.11) and $^{143}Nd/^{144}Nd$ (~0.5115) ratios, which are all compatible with the felsic derivation of their protoliths. The ratios yielded depleted mantle model ages ranging from 2.29 to 2.33 Ga, and all samples have positive $\varepsilon_{Nd}(t)$ values ranging from +1.1 to +1.8. These results are similar to those reported by Klein et al. (2005a) for the type locality of the complex (Appendix A) and, in combination with zircon geochronological data indicate derivation from juvenile protoliths with limited, if any, Archean contribution. However, sample EK274 (garnet-bearing metatonalite) revealed a slightly higher $^{147}Sm/^{144}Nd$ ratio of 0.13, which implies a model age of 2.63 Ga and $\varepsilon_{Nd}(t)$ value of −1.3, which would suggest larger participation of Archean crust in the magma. It is possible to argue that this $T_{DM}$ model age was overestimated, because of the presence of garnet. However, the garnet content is similar (about 1%) to that observed in sample EK311A (metatonalite), despite the different model age. Using the double stage method of calculating the depleted mantle model age, and assuming the $^{147}Sm/^{144}Nd$ average value of 0.11 for the upper continental crust (Rudnick and Gao, 2005) a value of 2.50 Ga is obtained.

Regarding the Rhyacian granitoids, a sample from the ferroan Canoa quartz diorite (EK37 - metatonalite) shows isotopic results very similar to those presented by the garnet-bearing biotite gneiss above (EK274), with Archean $T_{DM}$ ages of 2.62 Ga and 2.50 Ga, using the single and double stages methods, respectively, and $\varepsilon_{Nd}(t)$ value of −1.0. Therefore, although these results should be treated with caution, it is more likely that higher proportions of Archean crust have been involved in the magma source of the protoliths of samples EK274 and EK37.

The Nd isotope compositions of the Rhyacian amphibolites, the Muriá and Cocal units, are compatible with those expected for mafic rocks. The amphibolites show slightly (Muriá, +0.4 to +1.8), and moderately to strongly positive $\varepsilon_{Nd}(t)$ values (Cocal, +5.6 to +8.0). Single and double stage model ages are respectively ~2.80 Ga and ~2.30 Ga for the Muriá amphibolite, 1.0 Ga and 1.85 to 2.01 Ga for the Cocal amphibolite. The Cocal samples, in both calculation methods, present model ages that are lower than the crystallization age, and are geologically irrelevant. Considering the $\varepsilon_{Nd}(t)$ values, it is likely that the Paleoproterozoic model ages of Muriá represent better the crust residence time of the basic protoliths. However, mafic and ultramafic rocks are not suitable for model (crust formation) age calculations, because the evolution of the Sm/Nd ratio through time is sub-parallel to the evolution line of the chondritic reservoir (e.g., Dickin, 2005). Therefore, even the model ages of Muriá must be taken with caution.

Two samples of the Neoproterozoic calc-alkaline intrusion (Caramujinho metamicrotonalite) show similar isotopic results, which define the $T_{DM}$ age of 2.25 Ga, and strongly negative $\varepsilon_{Nd}(t)$ values of −15.7 and −14.4. These indicate the major influence of Paleoproterozoic crustal sources in the protoliths, which is in line with the ages of inherited zircon (Appendix E, and Fig. 11J).

The isotopic parameters of the Neoproterozoic peraluminous Pantoja Granite are slightly outside the normal values expected for unfractionated felsic rocks. Single and double stage model ages are quite different, 2.54 and 2.05 Ga, respectively, and the $\varepsilon_{Nd}(t)$ value is −12.2. Nevertheless, both values indicate strong participation of old (Mesoproterozoic, Paleoproterozoic, Archean) sources in the origin of the granitic magma, which is in line with the zircon data.

## 7. Discussions

### 7.1. Timing and types of magmatic episodes in the Gurupi Belt

Our results, together with available literature, allow establishing the sequence of magmatic events that occurred in what became the Gurupi Belt, the interpretation of the tectonic settings in which these events occurred, during at least two orogenic cycles, and in an extension-related episode, and the investigation of the juvenile versus reworked character of the magma sources (Figs. 12 and 13, and Appendix A).

**Table 1**
New Sm–Nd isotope results for magmatic rock units of the Gurupi Belt (a compilation of published data is presented in Appendix A).

| Sample | Rock type | Age (Ma) | Sm (ppm) | Nd (ppm) | Sm/Nd | $f$ (Sm/Nd)[a] | $^{147}Sm/^{144}Nd$ | $^{143}Nd/^{144}Nd$ | $2\sigma$ ($10^{-6}$) | $\varepsilon_{Nd}$ (0) | $\varepsilon_{Nd}(t)$ | $T_{DM}$ (Ga) | $T_{DM}$ DS (Ga) |
|---|---|---|---|---|---|---|---|---|---|---|---|---|---|
| Itapeva Complex | | | | | | | | | | | | | |
| EK163A | Bt gneiss | 2148 | 7.186 | 37.534 | 0.19145 | −0.411 | 0.1157 | 0.511574 | 8 | −20.76 | +1.8 | 2.29 | – |
| EK53A | Bt gneiss | 2167 | 1.261 | 6.706 | 0.18804 | −0.422 | 0.1137 | 0.511518 | 10 | −21.85 | +1.2 | 2.33 | – |
| EK274 | Bt metatonalite (gnt) | 2160 | 4.441 | 20.100 | 0.22095 | −0.321 | 0.1336 | 0.511671 | 6 | −18.87 | −1.3 | 2.63 | 2.52 |
| EK311A | Ep-bt metatonalite (gnt) | 2149 | 3.322 | 17.660 | 0.18811 | −0.422 | 0.1137 | 0.511522 | 14 | −21.78 | +1.1 | 2.33 | – |
| Tromaí Intrusive Suite | | | | | | | | | | | | | |
| EK24 | Monzogranite | 2160 | 4.568 | 20.081 | 0.22748 | −0.300 | 0.1375 | 0.511889 | 13 | −14.6 | +1.8 | 2.32 | 2.30 |
| Canoa quartz-diorite | | | | | | | | | | | | | |
| EK37 | Metatonalite | 2162 | 8.707 | 38.270 | 0.22751 | −0.301 | 0.1375 | 0.511744 | 16 | −17.44 | −1.0 | 2.62 | 2.50 |
| Caramujinho metamicrotonalite | | | | | | | | | | | | | |
| EK32 | Metamicrotonalite | 624 | 3.925 | 22.328 | 0.17579 | −0.459 | 0.1063 | 0.511466 | 5 | −22.9 | −15.7 | 2.25 | 2.32 |
| EK35 | Metamicrotonalite | 624 | 3.076 | 16.505 | 0.18637 | −0.427 | 0.1113 | 0.511559 | 20 | −21.0 | −14.4 | 2.25 | 2.22 |
| Pantoja Granite | | | | | | | | | | | | | |
| EK41 | Bt-mus granodiorite | 597 | 2.74 | 12.01 | 0.228 | −0.298 | 0.1380 | 0.511789 | 9 | −16.56 | −12.2 | 2.54 | 2.05 |
| Muriá Amphibolite | | | | | | | | | | | | | |
| EK31 | Amphibolite | 2136 | 1.506 | 4.695 | 0.32077 | −0.014 | 0.1939 | 0.512692 | 14 | +1.1 | +1.8 | 2.80 | 2.29 |
| EK41 | Amphibolite | 2136 | 1.877 | 6.537 | 0.28713 | −0.117 | 0.1736 | 0.512331 | 10 | −6.0 | +0.4 | 2.76 | 2.39 |
| Cocal Amphibolite | | | | | | | | | | | | | |
| EL122A | Amphibolite | 2162 | 1.808 | 6.079 | 0.29742 | −0.083 | 0.1804 | 0.512814 | 26 | +3.4 | +8.0 | 1.05 | 1.85 |
| EL141 | Amphibolite | 2166 | 3.424 | 10.449 | 0.32769 | 0.007 | 0.1981 | 0.512944 | 11 | +6.0 | +5.6 | 0.98 | 2.01 |

Mineral abbreviations: ep–epidote, bt–biotite, gnt–garnet, mus–muscovite.
DS: Double-stage.
[a] $f$ (Sm/Nd) = ($^{147}Sm/^{144}Nd_{sample}$/0.1967)-1 (Nelson and DePaolo, 1985).

The main period of magmatism in the exposed Gurupi Belt, in terms of volume, was the Rhyacian and the events can be grouped into (1) subduction-related pre-collisional plutonic suites and volcano-sedimentary basin, (2) syn- to late-collisional, strongly peraluminous plutonic suites, and (3) late- to post-collisional, potassic plutonic suites (Fig. 12, and Appendix A). After the Rhyacian, magmatic activity was recorded only in the Tonian, with the extension-related alkaline intrusion, and in the Ediacaran, with limited calc-alkaline and peraluminous intrusions.

**ca. 2185–2130 Ma** – The pre-collisional suites include the calc-alkaline magnesian gneiss and granitoid/metagranitoids units (Itapeva, Tromaí) to subordinately ferroan granitoids (Canoa), the potassic granites (Cantão, Jonasa), and the tholeiitic to calc-alkaline mafic intrusions (Muriá and Cocal amphibolites) formed between 2179 ± 18 and 2166 ± 19 Ma. The subduction-related plutonic rocks formed in island arcs to which are associated with the metavolcano-sedimentary sequence of the Chega Tudo Formation. These associations were responsible for the construction of arc systems that are in physical continuity with coeval rocks of the São Luís cratonic fragment, and represent the accretionary phase of the Rhyacian orogeny.

The juvenile Tromaí Suite (2179–2144 Ma), with high Ba–Sr signature, and tonalitic and normal calc-alkaline varieties, is chemically slightly different from the Tromaí Suite of the São Luís cratonic fragment (Figs. 5 and 6; Klein et al., 2008), indicating some variation in the whole expanded suite. The suite shares some similarities with coeval quartz-diorites and granodiorites, respectively, described in the West African Craton (Ghana) by Block et al. (2016), and with juvenile, high-Sr-Ba suites of the Siderian-Rhyacian Mineiro Belt in the southern portion of the São Francisco Craton (e.g., Moreira et al., 2018). These suites are also interpreted do be formed in subduction-related systems. In fact, the Tromaí Suite in the Gurupi Belt fills a compositional gap, with $SiO_2$ concentrations intermediate to those presented by rocks occurring in the cratonic area, and falls within the Rb/Zr range of primitive arc (Fig. 13A). The Muriá amphibolite is associated with this magmatic stage.

The Canoa quartz diorite (2173–2151 Ma), which is a novelty found in this study, forms part of the same batholith of the Tromaí Suite, but presents different chemical (calcic-ferroan), and Nd isotope signature (Table 1 and Fig. 12). As a whole, the concentrations of, and relationships between trace elements indicate the tendency to a within-plate tectonic setting for the Canoa quartz diorite, or for the sources of its magmas (Fig. 4). The chemical signature is also, in general, compatible with that of A-type granites (e.g., Whalen et al., 1987). However, as part of the same batholith of the Tromaí Suite, anorogenic settings are unlikely for Canoa. It is also worth noting that the ferroan calcic signature is extremely rare in the literature. This rarity is because rocks of this composition form only as a result of very low-pressure fractionation of basalt and there are few environments that met this condition, with few examples referring to shallow and subordinate bodies associated with layered mafic intrusions or mafic dike systems (Frost and Frost, 2011, 2013), which seems not to be the case here. Another example is the ca. 1.9 Ga-old suite of tonalite and minor quartz diorite/gabbro from early juvenile arcs in the Canadian Flin Flon belt (Whalen et al., 2016). This rock association and some geochemical features of the Canoa quartz diorite, including the low $K_2O$ contents (~1.1%), the low Sr/Y (11), Rb/Sr (0.07) and Rb/Zr (0.4; primitive arc range) ratios (Fig. 13), and Nb–P–Ti depletions resemble those of the Flin Flon ferroan calcic granitoids. Whalen et al. (2016) interpreted this type of magmatism as emplaced within a thin crustal setting, probably subaqueous, associated with local extension in a convergent setting.

Additional evidence for the extension hypothesis comes from the metavolcano-sedimentary Chega Tudo Formation, which is spatially and temporarily associated with the subduction-related Tromaí Suite, and with the Canoa quartz diorite (Fig. 2). The volcanic rocks of this formation show association of felsic, intermediate, and mafic rocks, with variable chemical characteristics, from volcanic arc to intraplate (Fig. 7), in a relatively restricted area, and juvenile signature. These

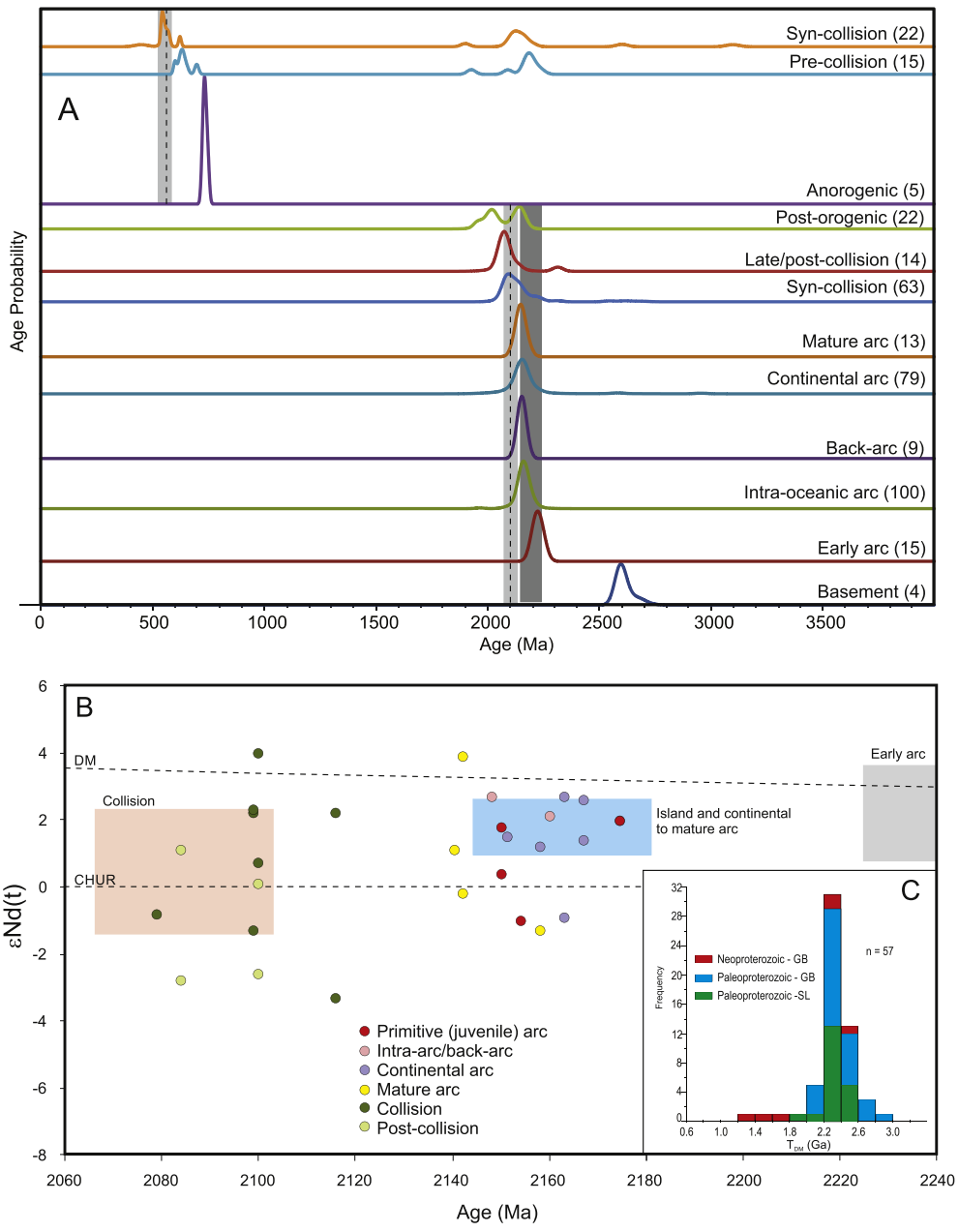


**Fig. 12.** (A) Composite relative probability diagram for crystallization age of zircons from magmatic rocks of the Gurupi belt (including this study) and São Luís cratonic fragment, separated by individual magmatic association. The grey vertical bars stand for the accretionary (dark grey) and collision (light grey) phases of the orogenies, whilst the vertical dashed lines correspond to the timing of metamorphism. Figures in parentheses represent the number of zircon grains used to draw each probability distribution plot. (B) Crystallization age versus $\varepsilon_{Nd}(t)$ diagram of igneous rocks from the Gurupi Belt. The colored polygons show the fields of the sequential evolutionary phases defined for the São Luís cratonic fragment by Klein et al. (2005b). Errors are ±7 Ma for the ages, and ±1 for the $\varepsilon_{Nd}$ values. The dashed lines stand for the evolution of the chondritic uniform reservoir (CHUR) and depleted mantle (DM). (C) Frequency histogram Sm–Nd $T_{DM}$ model ages of igneous rocks from the Gurupi Belt and São Luís cratonic fragment. Compilation of data and references in Appendix A.

characteristics strongly favor an orogenic setting for the metavolcanic rocks of the Chega Tudo Formation, and the volcanic and sedimentary contents are consistent with both intra- and back-arc basins (e.g., Ingersoll, 2012; Draut and Clift, 2013). The characteristics are similar to those described for the Ashanti belt of the West-African Craton and interpreted to be formed in an orogenic basin (Dampare et al., 2008; Block et al., 2016). Additionally, and based on the chemical similarity between the calc-alkaline andesites (Fig. 8) and the calc-alkaline tonalites of the Tromaí Suite (Fig. 5), it is possible that the andesites might represent volcanic equivalents of the tonalites.

The Itapeva Complex is comprised of two geochemically different and sequential magmatic pulses (orthogneisses of 2170–2144 Ma and garnet-bearing metatonalite of 2157–2141 Ma, not separated in maps to date). The oldest group only resembles chemically some granodiorites of the Tromaí Suite of the São Luís cratonic fragment (Figs. 4 and 5, described in Klein et al., 2008, and Fig. 6), but with zircon inheritance and slightly different Nd signature. Even within the oldest group of orthogneisses, the ages of the two dated samples (2167 ± 3 and 2148 ± 4 Ma, Appendix A) do not overlap within uncertainties, and there is some scattering in the distribution of $SiO_2$ versus Rb/Zr compositions (Fig. 13A), which collectively indicate more than one single plutonic type in this group of the complex. Therefore, we interpret the orthogneisses of the Itapeva magmatism as coeval, but distinct from the Tromaí magmatism (at least distinct sources and petrogenetic evolution). The metatonalites of the complex, despite age overlapping, are chemically distinct from both Itapeva orthogneisses and Tromaí granitoids (Figs. 4 and 5).

The Cantão and Jonasa granites (described in Palheta et al., 2009 and Klein et al., 2012) also differ chemically from Tromaí (and Itapeva orthogneisses) and probably represent continental arc plutonic suites, with Jonasa being interpreted as the mature arc phase (Fig. 13).

**ca. 2125–2070 Ma** – This period is characterized by the emplacement of a number of strongly peraluminous, two-mica granites, which form an NW–SE corridor parallel to the main structural grain of the Gurupi Belt (Fig. 2). These granites have clear (geochemical, geochronological, and isotopic) characteristics of crust-derived magmas and have been interpreted to mark the collisional phase of the Rhyacian orogeny in

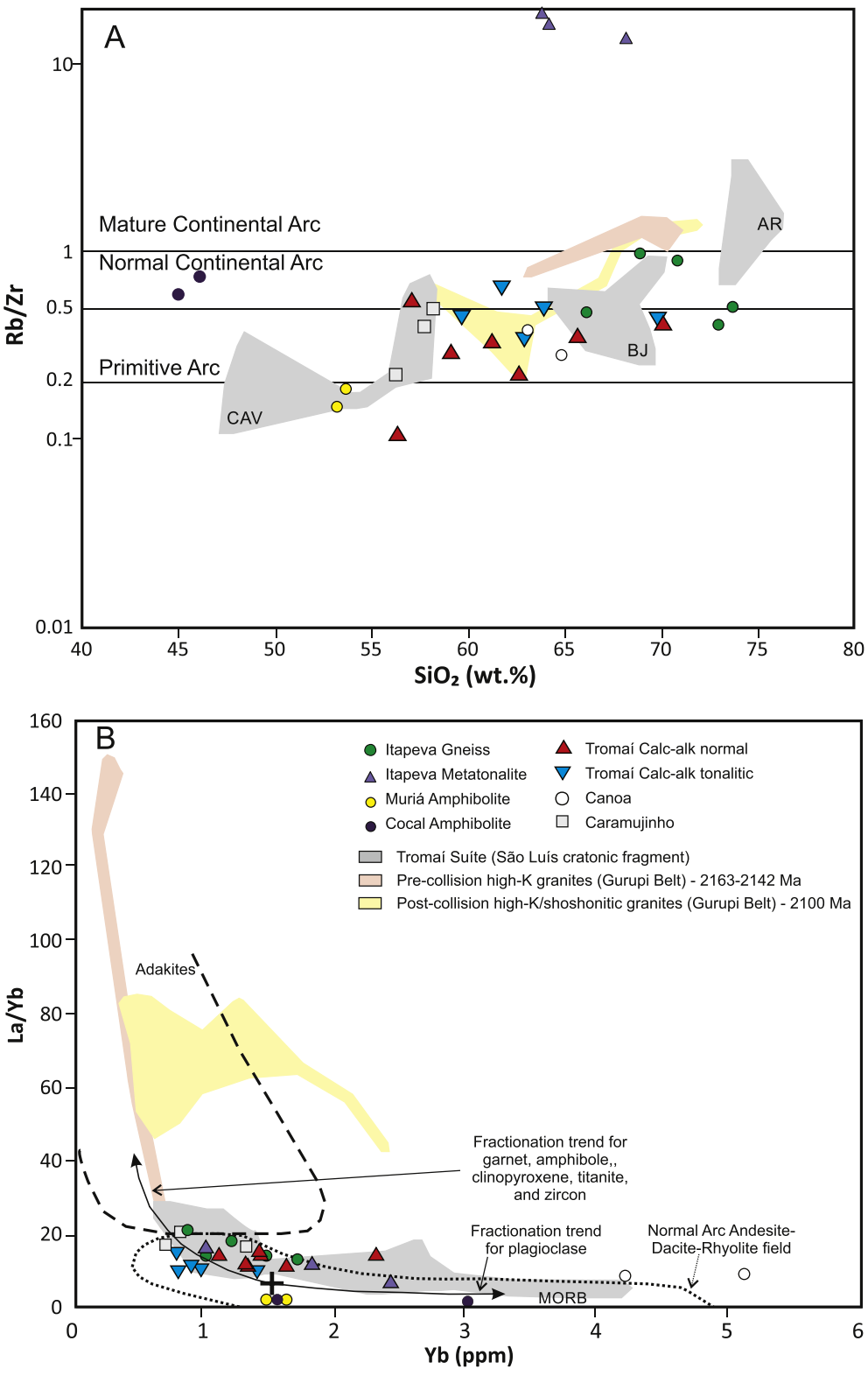


**Fig. 13.** Compositional variation diagrams (A) $SiO_2$ vs. Rb/Zr, and (B) Yb vs. La/Yb for Rhyacian plutonic associations of the Gurupi Belt (samples of the Neoproterozoic calc-alkaline intrusion – Caramujinho - are shown for comparison). Symbols (circles and triangles) represent data from this study; colored shaded fields stand for associations of the São Luís cratonic fragment (CAV – Cavala tonalite, BJ – Bom Jesus granodiorite, AR – Areal granite; Klein et al., 2008), and Gurupi Belt (Klein et al., 2012). In (A), the Rb/Zr limits for mature and normal continental arc, and primitive island arc plutonic suites are from Brown et al. (1984). In (B), compositional fields and fractionation trends as compiled by Richards and Kerrich (2007), and the cross stands for average medium-K andesite.

the region (Klein et al., 2012). In this study, we maintain this interpretation and added more dated plutons to this set. Potassic to shoshonitic granites and quartz-syenite also intruded in the same corridor (Fig. 2) and, although partially overlap in time with the collision-type granites, they represent late- to post-collision intrusions.

**ca. 730 Ma** – After the Rhyacian, the first magmatic record is represented by the intrusion of the nepheline syenite of 732 ± 7 Ma (Klein et al., 2005a). This alkaline intrusion indicates the existence of extensional (rift) phase in the Tonian period, which is also supported by detrital zircons of ca. 1100 Ma in the metasedimentary sequence (Gurupi Group) that is the possible wall rock for the intrusion (Klein et al., 2005a).

However, it is possible that a Mesoproterozoic magmatic event around 1400 Ma might have occurred in the Gurupi Belt. Zircons of this

age were found as inherited crystals in the crust-derived Neoproterozoic peraluminous granite (Pantoja, Fig. 11M), and in the detrital record of the siliciclastic Ediacaran–Cambrian Piriá Formation (Lopes et al., 2016). This magmatism may be still hidden in the region, or eroded away, or, alternatively, the sources of zircons were external to the belt.

**ca. 625 Ma** – Small bodies of calc-alkaline microtonalite represent this phase. The tectonic setting is uncertain (see the Neoproterozoic evolution section below), but we interpret this magmatism as the product of crustal reworking, which is given by the high number of inherited Rhyacian zircons and the Sm–Nd model ages (ca. 2.2 Ga), whereas the calc-alkaline characteristic was inherited from the source rocks.

**ca. 600–550 Ma** – The youngest magmatic event is also of small (known) volumetric expression and comprises the peraluminous, two-mica granites (Pantoja and Ney Peixoto). We could not bring more accuracy for this period dating sample EK41 of the Pantoja Granite, because of the large error. So, it is uncertain if the two peraluminous bodies represent one (which is more likely) or two magmatic events. Whole-rock geochemistry (Villas and Sousa, 2007) and geochronology (Palheta et al., 2009, and this study) indicate crustal origin (metasedimentary sources), and a post-collisional signature, at least for the Ney Peixoto Granite.

### 7.2. Rhyacian evolution

Previous works described the Paleoproterozoic evolution of the Gurupi Belt and the adjoining São Luís cratonic fragment as comprising of: (1) 2240 Ma – early island ± back-arc system, (2) ca. 2160–2150 Ma – main intra-oceanic ± back-arc system; (3) ca. 2160–2140 Ma – transitional to continental and mature arc system, (4) 2115–2085 Ma – collision magmatism, and (5) 2120–2080 Ma – late- to post-collision magmatism (Klein et al., 2008, 2009, 2012). All phases are present in the São Luís cratonic fragment, whilst the first (early) phase and the intra-oceanic arc of phase "2" have not been detected in the Gurupi Belt to date.

In this work, the five steps are maintained, but we broadened and improved the internal knowledge of each step (including better constraints on the age intervals for each stage), except for the early arc phase, which is still absent in the Gurupi Belt (Fig. 14A). The intra-oceanic phase is represented by the Tromaí Suite and the Muriá amphibolite (Fig. 14B). Extension during this phase (Fig. 14C) might be related to slab retreat, with concomitant opening of a back-arc basin (e.g., Uyeda and Kanamori, 1979) that housed the Chega Tudo volcano-sedimentary sequence, and also allowed the emplacement of the Canoa quartz diorite. The age of the closure of this basin is still uncertain and depends on additional studies.

The transitional and continental (normal and mature) arc systems are represented by more siliceous and potassic rocks, including the protoliths of the orthogneisses (normal arc) and metatonalites (mature arc) of the Itapeva Complex, along with the Cantão (normal arc) and Jonasa (mature arc) granites, also indicating the approximation of the arc systems to an older continental mass to the south (given by older $T_{DM}$ ages and limited inherited zircons – Fig. 12 and Appendix A). The collisional phase of the orogen is materialized by the production of crustal, peraluminous, *S*-type granites and limited migmatization, probably in response heating due to crustal thickening, which was followed by the emplacement of post-collisional, K-rich granites (Fig. 14D).

Therefore, the Rhyacian deformation and metamorphism in the Gurupi Belt are broadly constrained by this collision phase. The peraluminous granites intruded during $D_1$, indicating ca. 2100 Ma as the age of metamorphism and of this deformation phase. The leucogranite veins (migmatization?) of 2092 ± 20 Ma, included in the gneisses of the Itapeva Complex were folded by $D_{1b}$, whereas the emplacement of the K-rich Timbozal Granite, which is not significantly deformed, at 2084 ± 5 Ma, places a lower limit for the $D_1$ event as a whole.

Another point to highlight is the broad zonation of the Rhyacian magmatic activity, with the intra-oceanic suites occurring to the northeast, followed by the continental arc, and then collisional suites to the southwest (Figs. 2 and 14). This suggests the existence of an older

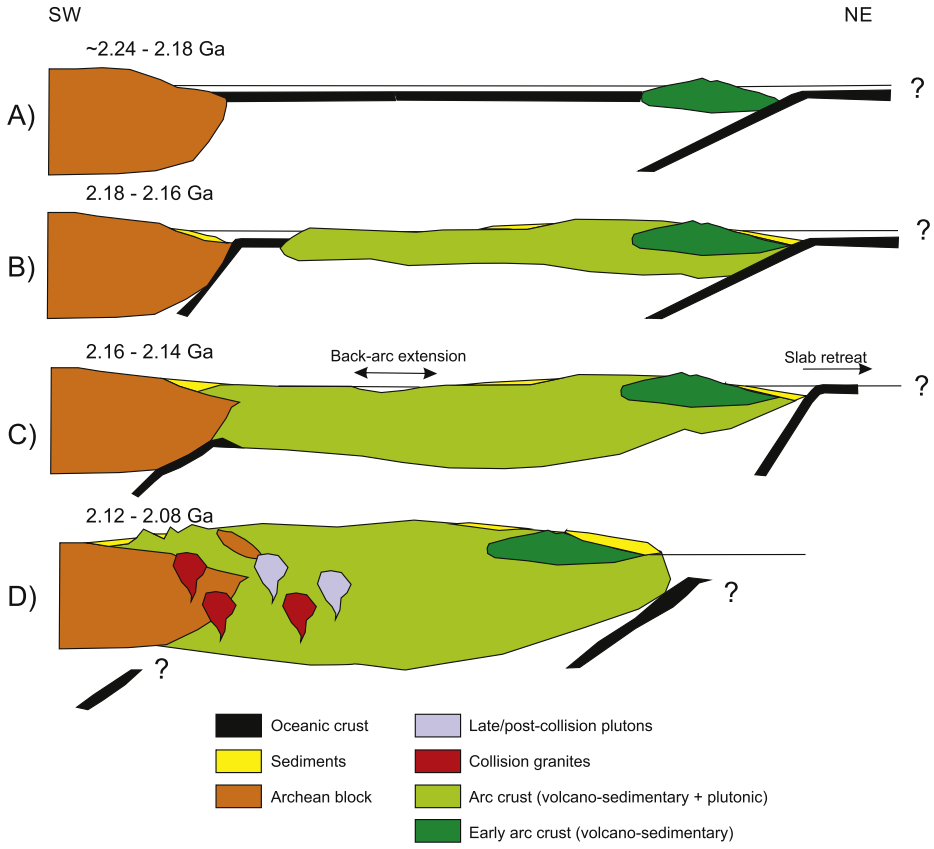


**Fig. 14.** Schematic (not to scale) model of the Rhyacian evolution. (A) Oceanization, subduction initiation and production of the early arc rocks (not present in the Gurupi Belt, only in the São Luís cratonic fragment). (B) Growing of the juvenile arc crust, with voluminous calc-alkaline and high Sr–Ba, and subordinate tholeiitic magmatism. (C) Coupled back-arc extension and slab retreat, and continuation of arc (essentially juvenile) maturation. (D) Arc-continent collision and magmatism induced by crustal thickening and metamorphism.

(Archean) continental block to the southwest (Parnaíba block or Amazonian Craton, Figs. 1 and 14).

### 7.3. Neoproterozoic–Cambrian evolution

Klein et al. (2005a) interpreted the Neoproterozoic evolution of the Gurupi Belt as consisting of (1) breakup of the Rhyacian block (São Luís-West Africa) and rift formation before 732 Ma, as suggested by the emplacement of the nepheline syenite pluton; (2) sedimentation with detritus coming from Archean, Paleoproterozoic, Mesoproterozoic, and Neoproterozoic sources; (3) closure of the basin at the end of the Neoproterozoic (580–550 Ma), as part of the Brasiliano/Pan-African cycle of orogenies. We have no additions regarding the first two phases. Klein et al. (2005a) considered two possible evolution models for the rift: (1) aborted continental rift, characterizing an intracontinental orogen; (2) a continental margin/oceanic basin formed as spreading followed after rifting, with subsequent development of subduction and collision. Despite the scarcity of Neoproterozoic magmatism, the second hypothesis was emphasized because of the large number of detrital zircons from an immature (proximal) sandstone with ages in the 600–650 Ma range (Pinheiro et al., 2003). This fact was used to infer that felsic to intermediate magmatism has to some extent occurred in the region around this age and that this magmatism might be concealed beneath the Phanerozoic cover, or might have already been eroded away. The presence of outcropping Neoproterozoic rocks metamorphosed to the amphibolite facies (nepheline syenite) justify the removal of part of the overlying crust by erosion. In addition, the Gurupi Belt has been included in the proposition of a very long (~2500 km) Ediacaran continental subduction-collision system that participated of the amalgamation of the West Gondwana supercontinent (Ganade de Araujo et al., 2014).

This understanding is reviewed here. Despite its modest surface exposure, and despite the fact that part of the Gurupi Belt lies indeed beneath the Phanerozoic cover to the south (e.g., Brito Neves et al., 1984; Nunes, 1993; Klein et al., 2005a; Castro et al., 2014; Daly et al., 2014), we have no evidence of formation of oceanic crust or of arc/subduction systems in the Neoproterozoic, since the Gurupi Belt lacks Neoproterozoic ophiolites, magmatic arcs, subduction complexes, high-pressure metamorphism. Only relatively small bodies of Neoproterozoic *S*-type granites are present, nevertheless indicating that crustal melting was also limited. Furthermore, most of the exposed Gurupi Belt comprises reworked portions of the Rhyacian terrane (present-day São Luís cratonic fragment). Therefore, our data do not support neither the Neoproterozoic oceanization indicated by Klein et al. (2005a), nor the deep continental subduction suggested by Ganade de Araujo et al. (2015) for the Gurupi Belt region.

However, metamorphism and deformation are present at variable degrees in igneous and sedimentary rocks formed in the Neoproterozoic (Klein et al., 2005a; Tavares et al. (in review)). Greenschist to amphibolite metamorphic conditions prevailed in the Neoproterozoic. This metamorphism post-dates the intrusion of the metamorphosed Caramujinho microtonalite at ca. 624 Ma, and is broadly constrained by the K–Ar age of 580 ± 10 Ma on biotite from the nepheline syenite (Klein et al., 2005a and references therein), and by the lower intercept U–Pb age of 529 ± 43 Ma in titanite from the Cocal amphibolite. Lower intercept ages around 500 Ma (with large errors) have also been defined in samples dated in this study and in published works (e.g., Klein et al., 2005a, 2012), indicating Pb loss that we interpret as related to the Ediacaran–Early Cambrian metamorphism.

The vergence of fold axes indicates that the Neoproterozoic structures were produced in a compressive regime, with the maximum shortening vector $\sigma_1$ striking E–W (Tavares et al. in review). This orientation is similar to that described for the Araguaia Belt (Fig. 1B) 300 km to the west (Hasui et al., 1984). These lines of evidence indicate a Neoproterozoic/Cambrian orogenic event with mass transportation to the north, probably using the pre-existing $D_1$ and $D_2$ structures produced during the Rhyacian orogeny.

Since continental subduction/collision seems not to be the mechanism that induced tectonism in the Gurupi Belt, we come back to and improve the interpretation of Klein et al. (2005a) of an intracontinental orogeny (Fig. 15). The concealed Parnaíba block (Fig. 1) appears to be critical for constraining this orogenic model. This block has been inferred based on geophysics, petrography, and conventional Rb–Sr and K–Ar geochronology (Brito Neves et al., 1984; Cunha, 1986; Nunes, 1993). Limited information about the lithological content of the block indicates the presence of gneiss, granitoids, syenite, ignimbrite, trachyte, quartzite, sandstone, greywacke, mica schist, and phyllites (Cunha, 1986), i.e., rock types described in both the São Luís cratonic fragment and Gurupi Belt (Klein et al., 2005a, b). More recently, results of deep seismic reflection profiling (Daly et al., 2014) describes the Parnaíba block as a seismically homogeneous block, lacking apparent acoustic anisotropy, a response similar to that of the São Luís cratonic fragment, and that the Gurupi Belt represents a "deformation zone between the Parnaíba block and São Luís craton". These data and conclusions, reinforce our interpretation of a continuous Rhyacian block (São Luís-West Africa + Parnaíba) that was broken (rifted) in the Neoproterozoic (Tonian), forming a sedimentary basin that might have evolved to a margin of an epicontinental sea, and received limited igneous and predominantly sedimentary infill, closing in the Ediacaran–Cambrian.

As such, the Neoproterozoic–Cambrian evolution of the Gurupi Belt is more likely a reflex of orogenic events occurring elsewhere, in convergent margins peripheral to the Amazonian and West African cratons (Fig. 15A), as part of the Brasiliano-Pan African cycle of orogenies (Fig. 1), such as the Araguaia Belt (Alvarenga et al., 2000; Hodel et al., 2019) and the Borborema Province (Almeida et al., 1981) in Brazil, and their counterparts in West Africa, the Rockelide and Dahomeyde belts (Villeneuve, 2008; Guillot et al., 2019, and references therein). Intracontinental reworking is facilitated by pre-existing mechanical defects (Holdsworth et al., 2001), i.e., weak regions, and refertilized subcontinental lithosphere (Sheppard et al., 2010), which in the Gurupi region is explained by deformation and pronounced subduction during the Rhyacian orogeny. In addition, despite the intracontinental character of the Neoproterozoic–Cambrian orogeny, some crustal thickening has taken place, which is given by the production and crystallization of the peraluminous two-mica granite (Ney Peixoto) at ca. 625 °C and 5 kbar (depth of 18 km according to Villas and Sousa, 2007). The intrusion of this crust-derived granite at 549 ± 4 Ma is in line with the estimated age of metamorphism (580–511 Ma).

### 7.4. Regional correlations and relevance for continental assembly and break-up

There is a large body of evidence indicating that the São Luís cratonic fragment and the contiguous Rhyacian portion of the Gurupi Belt (Figs. 1 and 2) are a small part of the West African Craton in pre-Atlantic Ocean opening (Klein and Moura, 2008, and references therein). All Rhyacian magmatic episodes identified in the Gurupi Belt (and São Luís cratonic fragment) and discussed above have been documented in the southern West African Craton as part of the Eburnean/Birrimian orogeny (Block et al., 2016; Grenholm et al., 2019).

According to Grenholm et al. (2019), the accretionary phase produced continental crust in an archipelago-style volcanic arc system, with juvenile domains being juxtaposed with older (Archean) continental fragments. This process was diachronous and zoned, with NW-directed (present-day orientation) indentation caused by regional plate motions. Furthermore, the $D_1$ deformational phase we described correlates in time (~2.09–2.08 Ga) and associated magmatic process (crustal thickening and production of two-mica granites) with what is interpreted for the West African Craton (McFarlane et al., 2019). A difference we observed in the Brazilian tip of the Gurupi-São Luís-West Africa continental mass is that, apparently, the whole set of events are present in a small area in Gurupi-São Luís.

This Rhyacian evolution is coeval to and has broadly the same

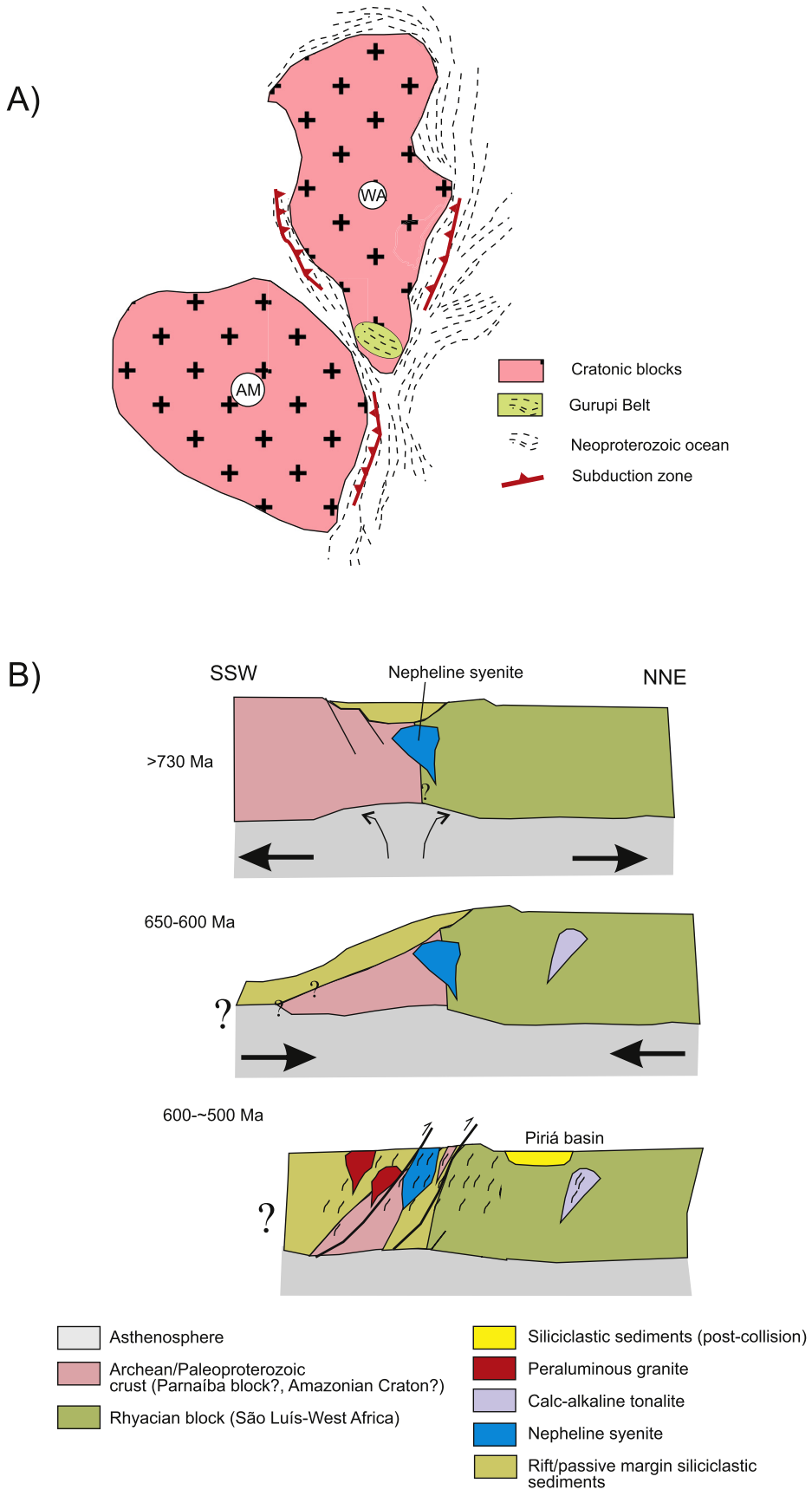


**Fig. 15.** Schematic (not to scale) model of the Neoproterozoic–Cambrian evolution. (A) Position of the Gurupi Belt in the Neoproterozoic in relation to Archean–Paleoproterozoic blocks and Brasiliano/Pan-African subduction zones. (B) Stages of Neoproterozoic magmatism recognized in the Gurupi Belt – pre-orogenic and syn- to late-orogenic.

duration of the Transamazonian cycle in South America, which is present in the Amazonian Craton as a major crust forming period (Santos et al., 2003). A difference is the absence of (known) high-grade (granulite facies) metamorphism in the Gurupi Belt, which is common at 2.10–2.08 Ga in the Amazonian Craton.

Paleomagnetic, geochronological, and geological evidence strongly suggest that Amazonia and West Africa (and in consequence Gurupi-São Luís) were together, forming a single continental mass by 2000–1970 Ma (Bispo-Santos et al., 2014). However, the inclusion (Cordani et al., 2009; Nance et al., 2014) or not (Pisarevsky et al., 2014) of this landmass in the Columbia (or Nuna) supercontinent is not a consensus. Also debatable is the participation (Cawood et al., 2016) or not (Cordani et al., 2003; Oriolo et al., 2017), of the Paleoproterozoic landmass in Rodinia. However, our data and knowledge about the Gurupi Belt events do not allow us to contribute to this discussion.

Finally, the fact is that continental breakup (rifting) in the Gurupi Belt region initiated sometime before 732 Ma (age of the nepheline syenite intrusion), and orogenic closure occurred at about 549 Ma (age of the intrusion of crust-derived peraluminous granites). These "end-member" ages are coincident with Rodinia breakup starting at ca. 760 Ma (Cawood et al., 2016), and the assembly of West Gondwana at 575–480 Ma (Schmitt et al., 2018), respectively. However, as we discussed in the previous section, the Neoproterozoic–Cambrian evolution of the Gurupi Belt was an intracontinental reflex of tectonic processes that took place at the margins of the Amazonian and West African paleoplates, having no direct role at least in Rodinia disintegration or in the amalgamation of Gondwana.

## 8. Conclusions

In this work, using field, petrographic, geochemical, geochronological (U–Pb), and isotopic (Sm–Nd) data on magmatic associations, along with the revaluation of published information, we broadened the knowledge about the poly-phase tectonic evolution of the Gurupi Belt. The following magmatic events, with respective tectonic settings, are recognized in the Rhyacian (main period of crust formation), and in the Neoproterozoic (limited magmatism, but considerable tectonic reworking).

(1) 2185–2130 Ma – Juvenile, subduction-related granitoids and minor mafic intrusions (now amphibolites), formed in intra-oceanic and continental arcs, and volcano-sedimentary sequence deposited in intra- or back-arc setting.
(2) 2125–2070 Ma – Strongly peraluminous two-mica granites and potassic/shoshonitic granitoids and quartz syenite produced during crustal thickening and collision, and associated with greenschist to amphibolite facies metamorphism, local migmatization, and $D_1$ compressive and progressive deformation.

The spatial distribution of the magmatic associations indicate subduction from NE to SW (present-day configuration), and the existence of a continental margin (Archean block?) to the southwest. The associations are in physical continuity with the terranes of the São Luís cratonic fragment to the north, and the orogenic scenario correlates with what is observed in the West African Craton (Eburnean/Birrimian terranes).

(3) 730 Ma – Extension, rifting, and intrusion of an anorogenic nepheline syenite (now gneiss).
(4) 625 Ma – Localized calc-alkaline plutonism (now metatonalite) of crustal origin.
(5) 600–550 – Localized peraluminous, two-mica granites formed during crustal thickening, broadly coeval with greenschist to amphibolite facies metamorphism, $D_3$ deformation, and closure of the rift.

We interpret the Neoproterozoic evolution as an intracontinental process, a distal consequence of orogenic events occurring in the periphery of the West African and Amazonian cratons, which led to the assembly of West Gondwana. Being intracontinental, the Neoproterozoic orogeny in the Gurupi Belt bears no role in Gondwana agglutination.

## Declaration of competing interest

The authors declare that they have no known competing financial interests or personal relationships that could have appeared to influence the work reported in this paper.

## Acknowledgements

This paper is mostly an outcome of institutional projects developed by CPRM/Geological Survey of Brazil in the Gurupi Belt, with the additional support of the Brazilian "Conselho Nacional de Desenvolvimento Científico e Tecnológico" (CNPq) to the first author (research grant 306798/2016-6). Kotaro Uchigasaki and Luisa Sousa (CPRM) are thanked for helping with zircon imagery and figures. The authors acknowledge the insightful comments and criticisms of two GSF anonymous reviewers and from the Editor (Nick Roberts), which allowed us to improve the manuscript.

## Appendix A. Supplementary data

Supplementary data to this article can be found online at https://doi.org/10.1016/j.gsf.2020.02.016.

## References

Abreu, F.A.M., Lesquer, A., 1985. Consideracções sobre o Pré-Cambriano da região sul-sudoeste do Cráton São Luís. In: 2nd Simpósio de Geologia da Amazônia, Anais, vol. 1, pp. 7–21 (in Portuguese).
Almeida, F.F.M., Hasui, Y., Brito Neves, B.B., 1976. The upper Precambrian of South America. Boletim Instituto de Geociências USP 7, 45–80.
Almeida, F.F.M., Hasui, Y., Brito Neves, B.B., Fuck, R.A., 1981. Brazilian structural provinces: an introduction. Earth Sci. Rev. 17, 1–21.
Alvarenga, C.J.S., Moura, C.A.V., Gorayeb, P.S.S., Abreu, F.A.M., 2000. Paraguay and Araguaia belts. In: Cordani, U.G., Milani, E.J., Thomaz Filho, A., Campos, D.A. (Eds.), Tectonic Evolution of South America. Rio de Janeiro.
Bettencourt, J.S., Borges, W.R., Koritiake, M., 1991. The Cachoeira gold deposit, Gurupi Belt, Para, Brazil: geological setting, structure and mineralization — a preliminary report. In: Ladeira, E.A. (Ed.), Brazil Gold'91. Balkema, pp. 203–208.
Bispo-Santos, F., D'Agrella-Filho, M.S., Janikian, L., Reis, N.J., Trindade, R.I.F., Reis, M.A.A.A., 2014. Towards Columbia: Paleomagnetism of 1980–1960 Ma Surumu volcanic rocks, Northern Amazonian Craton. Precambrian Res. 244, 123–138.
Boynton, W.V., 1984. Cosmochemistry of the rare-earth elements: meteorite studies. In: Henderson, P. (Ed.), Rare-Earth Elements Geochemistry. Elsevier, Amsterdam, pp. 63–114.
Black, L.P., Kamo, S.L., Allen, C.M., Aleinikoff, J.N., Davis, D.W., Korsch, R.J., Foudoulis, C., 2003. Temora 1: a new zircon standard for Phanerozoic U-Pb geochronology. Chem. Geol. 200, 155–170.
Black, L.P., Kamo, S.L., Allen, C.M., Davis, D.W., Aleinikoff, J.N., Valley, J.W., Mundil, R., Campbell, I.H., Korsch, R.J., Williams, I.S., Foudoulis, C., 2004. Improved $^{206}Pb/^{238}U$ microprobe geochronology by the monitoring of a trace-element-related matrix effect; SHRIMP, ID-TIMS, ELA-ICP-MS and oxygen isotope documentation for a series of zircon standards. Chem. Geol. 205, 115–140.
Block, S., Baratoux, L., Zeh, A., Laurent, O., Bruguier, O., Jessell, M., Ailleres, L., Sagna, R., Parra-Avila, L.A., Bosch, D., 2016. Paleoproterozoic juvenile crust formation and stabilisation in the south-eastern West African Craton (Ghana); New insights from U-Pb-Hf zircon data and geochemistry. Precambrian Res. 287, 1–30.
Brito Neves, B.B., Fuck, R.A., 2014. The basement of the South American platform: half Laurentian (N-NW) + half Gondwanan (E-SE) domains. Precambrian Res. 244, 75–86.
Brito Neves, B.B., Fuck, R.A., Cordani, U.G., Thomaz Filho, A., 1984. Influence of basement structures on the evolution of the major sedimentary basins of Brazil: a case of tectonic heritage. J. Geodyn. 1, 495–510.
Brown, G.C., Thorpe, R.S., Webb, P.C., 1984. The geochemical characteristics of granitoids in contrasting arcs and comments on magma sources. J. Geol. Soc. London 141, 413–426.
Bühn, B., Pimentel, M.M., Matteini, M., Dantas, E.L., 2009. High spatial resolution analysis of Pb and U isotopes for geochronology by laser ablation multicollector inductively coupled plasma mass spectrometry (LA-MC-IC-MS). An Acad. Bras Ciências 81, 1–16.
Cabanis, B., Lecolle, M., 1989. Le diagramme La/10–Y/15–Nb/8: un outil pour la discrimination des series volcaniques et la mise en evidence des processus de

mélange et/ou de contamination crustale. CR Acad. Sci. Paris 309, 2023–2029 (in French).
Castro, D.L., Fuck, R.A., Phillips, J.D., Vidotti, R.M., Bezerra, F.H.R., Dantas, E.L., 2014. Crustal structure beneath the Paleozoic Parnaíba Basin revealed by airborne gravity and magnetic data, Brazil. Tectonophysics 614, 128–145.
Cawood, P.A., Strachan, R.A., Pisarevsky, S.A., Gladkouchub, D.P., Murphy, J.B., 2016. Linking collisional and accretionary orogens during Rodinia assembly and breakup: implications for models of supercontinent cycles. Earth Planet Sci. Lett. 449, 118–126.
Compston, W., Williams, I.S., Meyer, C., 1984. U-Pb geochronology of zircons from lunar breccia 73217 using a sensitive high mass-resolution ion-microprobe. J. Geophys. Res. 98B, 525–534.
Condie, K.C., 1987. Early Proterozoic volcanic regimes in southwestern North America. In: Pharaoh, T.C., Beckinsale, R.D., Rickard, D. (Eds.), Geochemistry and Mineralization of Proterozoic Volcanic Suites, vol. 33. Geological Society of London, Special Pub., pp. 211–218
Condie, K.C., 1997. Plate Tectonics and Crustal Evolution. Butterworth-Heinemann, London, p. 282.
Cordani, U.G., D'Agrella-Filho, M.S., Brito Neves, B.B., Trindade, R.I., 2003. Tearing up Rodinia: the Neoproterozoic palaeogeography. Terra. Nova 15, 350–359.
Cordani, U.G., Teixeira, W., D'Agrella-Filho, M.S., Trindade, R.I., 2009. The position of the Amazonian Craton in supercontinentes. Gondwana Res. 15, 396–407.
Cordani, U.G., Pimentel, M.M., Araujo, C.E.G., Basei, M.A.S., Fuck, R.A., Girardi, V.A.V., 2013. Was there an Ediacaran Clymene Ocean in central South America? Am. J. Sci. 313, 517–539.
Costa, J.L., 2000. Programa Levantamentos Geológicos Básicos Do Brasil. Programa Grande Carajás. Castanhal, Folha SA. 23-V-C. Estado Do Pará. Belém, CPRM (CD-ROM) (in Portuguese).
Costa, J.B.S., Hasui, Y., 1997. Evolução geológica da Amazônia. In: Costa, M.L., Angélica, R.S. (Eds.), Contribuições à Geologia da Amazônia, Belém, FINEP/SBG-NO, pp. 15–90 (in Portuguese).
Cunha, F.M.B., 1986. Evolução paleozóica da Bacia do Parnaíba e seu arcabouço tectônico. M.Sc. Thesis. Universidade Federal do Rio de Janeiro, Instituto de Geociências, p. 107 (in Portuguese).
Daly, M.C., Andrade, V., Barousse, C.A., Costa, R., Mcdowell, K., Piggott, N., Poole, A.J., 2014. Brasiliano crustal structure and the tectonic setting of the Parnaíba basin of NE Brazil: results of a deep seismic reflection profile. Tectonics 33, 1–19. https://doi.org/10.1002/2014TC003632.
Dampare, S.B., Shibata, T., Asiedu, D.K., Osae, S., Banoeng-Yakubo, B., 2008. Geochemistry of Paleoproterozoic metavolcanic rocks from the southern Ashanti volcanic belt, Ghana: petrogenetic and tectonic setting implications. Precambrian Res. 162, 403–423.
DePaolo, D.J., 1988. Neodymium Isotope Geochemistry. An Introduction. Springer-Verlag, Berlin, p. 187.
Dickin, A.P., 2005. Radiogenic Isotope Geology. New York, Cambridge, p. 492.
Draut, A.E., Clift, P.D., 2013. Differential preservation in the geologic record of intraoceanic arc sedimentary and tectonic processes. Earth Sci. Rev. 116, 57–84.
Foley, S.F., Wheller, G.E., 1990. Parallels in the origin of the geochemical signatures of island arc volcanics and continental potassic igneous rocks: the role of residual titanites. Chem. Geol. 85, 1–18.
Frost, C.D., Frost, B.R., 2011. On ferroan (A-type) granitoids: their compositional variability and modes of origin. J. Petrol. 52, 39–53.
Frost, C.D., Frost, B.R., 2013. Proterozoic ferroan feldspathic magmatism. Precambrian Res. 228, 151–163.
Ganade de Araújo, C.E., Rubatto, D., Hermann, J., Cordani, U.G., Caby, R., Basei, M.A.S., 2014. Ediacaran 2,500-km-long synchronous deep continental subduction in the West Gondwana Orogen. Nat. Commun. 5, 5198. https://doi.org/10.1038/ncomms6198.
Gioia, S.M.L.C., Pimentel, M.M., 2000. The Sm-Nd method in the geochronology laboratory of the University of Brasília. An Acad. Bras Ciências 72, 219–245.
Gorayeb, P.S.S., Gaudette, H.E., Moura, C.A.V., Abreu, F.A.M., 1999. Geologia e geocronologia da Suíte Rosário, nordeste do Brasil, e sua contextualização geotectônica. Rev. Bras. Geociencias 29, 571–578 (in Portuguese).
Grenholm, M., Jessell, M., Thébaud, N., 2019. A geodynamic model for the Paleoproterozoic (ca. 2.27–1.96 Ga) Birimian Orogen of the southern West African Craton – insights into an evolving accretionary-collisional orogenic system. Earth Sci. Rev. 192, 138–193.
Guillot, S., Agbossoumondé, Y., Bascou, J., Berger, J., Duclaux, G., Hilairet, N., Ménot, R.P., Schwartz, S., 2019. Transition from subduction to collision recorded in the Pan-African arc complexes (Mali to Ghana). Precambrian Res. 320, 261–280.
Halla, J., van Hunen, J., Heilimo, E., Hölttä, P., 2009. Geochemical and numerical constraints on Neoarchaean plate tectonics. Precambrian Res. 174, 155–162.
Harris, N.B.W., Pearce, J.A., Tindle, A.G., 1986. Geochemical characteristics of collision-zone magmatism. In: Coward, M.P., Ries, A.C. (Eds.), Collision Tectonics, vol. 19. Geological Society of London Special Publication, pp. 67–81.
Hastie, A.R., Kerr, A.C., Pearce, J.A., Mitchell, S.F., 2007. Classification of altered volcanic island arc rocks using immobile trace elements: development of the Th-Co discrimination diagram. J. Petrol. 12, 2341–2357.
Hasui, Y., Abreu, F.A.M., Villas, R.N.N., 1984. Província Parnaíba. In: Almeida, F.F.M., Hasui, Y. (Eds.), O Pré-Cambriano No Brasil. São Paulo, Edgard Blücher, pp. 36–45.
Hawkeswork, C.J., Powell, M., 1980. Magma genesis in the Lesser Antilles island arc. Earth Planet Sci. Lett. 51, 297–308.
Horstwood, M.S.A., Kosler, J., Gehrels, G., Jackson, S.E., McLean, N.M., Paton, C., Pearson, N.J., Sircombe, K., Sylvester, P., Vermeesch, P., Bowring, J.F., Condon, D.J., Schoene, B., 2016. Community-derived standards for LA-ICP-MS U-(Th-)Pb geochronology – uncertainty propagation, age interpretation and data reporting. Geostand. Geoanal. Res. 40 (3), 311–332.
Hodel, F., Trindade, R.I.F., Macouin, M., Meira, V.T., Dantas, E.L., Paixão, M.A.P., Rospabé, M., Castro, M.P., Queiroga, G.N., Alkmim, A.R., Lana, C.C., 2019. A Neoproterozoic hyper-extended margin associated with Rodinia's demise and Gondwana's build-up: the Araguaia Belt, central Brazil. Gondwana Res. 66, 43–62.
Holdsworth, R.E., Hand, M., Miller, J.A., Buick, I.S., 2001. Continental reactivation and reworking: an introduction. In: Miller, J.A., Holdsworth, R.E., Buick, I.S., Hand, M. (Eds.), Continental Reactivation and Reworking, vol. 184. Geological Society, London, Special Publications, pp. 1–12.
Hurley, P.M., Almeida, F.F.M., Melcher, G.C., Cordani, U.G., Rand, J.R., Kawashita, K., Vandoros, P., Pinson, W.H., Fairbairn, H.W., 1967. Test of continental drift by comparison of radiometric ages. Science 157, 495–500.
Ingersoll, R.V., 2012. Tectonics of sedimentary basins, with revised nomenclature. In: Busby, C., Pérez, A.Z. (Eds.), Tectonics of Sedimentary Basins: Recent Advances. Blackwell Publishing Ltd., pp. 3–43
Irvine, T.N., Baragar, W.R.A., 1971. A guide to the chemical classification of the common volcanic rocks. Can. J. Earth Sci. 8, 523–548.
Janousek, V., Farrow, C.M., Erban, V., 2006. Interpretation of whole-rock geochemical data in igneous geochemistry: introducing Geochemical Data Toolkit (GCDkit). J. Petrol. 47, 1255–1259.
Klein, E.L., 2014. Ore fluids of orogenic gold deposits of the Gurupi Belt, Brazil: a review of the physico-chemical properties, sources, and mechanisms of Au transport and deposition. In: Garofalo, P.S., Ridley, J.R. (Eds.), Gold-Transporting Hydrothermal Fluids in the Earth's Crust, vol. 402. Geological Society, London, Special Publications, pp. 121–145. https://doi.org/10.1144/SP402.2.
Klein, E.L., Lopes, E.C.S., 2011. Geologia e recursos minerais da folha Centro Novo do Maranhão – SA.23-Y-B-I, Estados do Maranhão e Pará, Escala 1:100,000. Belém, CPRM, 131 pp (in Portuguese).
Klein, E.L., Moura, C.A.V., 2001. Age constraints on granitoids and metavolcanic rocks of the São Luís craton and Gurupi belt, northern Brazil: implications for lithostratigraphy and geological evolution. Int. Geol. Rev. 43, 237–253.
Klein, E.L., Moura, C.A.V., 2003. Sintese geológica e geocronológica do Craton São Luís e do Cinturão Gurupi na região do rio Gurupi (NE-Para/NW-Maranhão). Revista Geologia USP, Série Científica 3, 97–112 (in Portuguese).
Klein, E.L., Moura, C.A.V., 2008. São Luís craton and Gurupi belt (Brazil): possible links with the West-African craton and surrounding Pan-African belts. In: Pankhurst, R.J., Trouw, R.A.J., Brito Neves, B.B., de Wit, M.J. (Eds.), West Gondwana: Pre-cenozoic Correlations across the South Atlantic Region, 294. Geological Society, London, Special Publications, pp. 137–151.
Klein, E.L., Moura, C.A.V., Krymsky, R., Griffin, W.L., 2005a. The Gurupi belt in northern Brazil: lithostratigraphy, geochronology, and geodynamic evolution. Precambrian Res. 141, 83–105.
Klein, E.L., Moura, C.A.V., Pinheiro, B.L.S., 2005b. Paleoproterozoic crustal evolution of the São Luís Craton, Brazil: evidence from zircon geochronology and Sm-Nd isotopes. Gondwana Res. 8, 177–186.
Klein, E.L., Luzardo, R., Moura, C.A.V., Armstrong, R., 2008. Geochemistry and zircon geochronology of Paleoproterozoic granitoids: further evidence on the magmatic and crustal evolution of the São Luís cratonic fragment, Brazil. Precambrian Res. 165, 221–242.
Klein, E.L., Luzardo, R., Moura, C.A.V., Lobato, D.C., Brito, R.S.C., Armstrong, R., 2009. Geochronology, Nd isotopes and reconnaissance geochemistry of volcanic and metavolcanic rocks of the São Luís Craton, northern Brazil: implications for tectonic setting and crustal evolution. J. S. Am. Earth Sci. 27, 129–145.
Klein, E.L., Rodrigues, J.B., Lopes, E.C.S., Soledade, G.L., 2012. Diversity of Rhyacian granitoids in the basement of the Neoproterozoic–Early Cambrian Gurupi Belt, northern Brazil: geochemistry, U–Pb zircon geochronology, and Nd isotope constraints on the Paleoproterozoic magmatic and crustal evolution. Precambrian Res. 220–221, 192–216.
Klein, E.L., Tassinari, C.C.G., Vasconcelos, P.M., 2014. U-Pb SHRIMP and $^{40}Ar/^{39}Ar$ constraints on the timing of mineralization in the Paleoproterozoic Caxias orogenic gold deposit, São Luís cratonic fragment, Brazil. Braz. J. Genet. 44, 277–288. https://doi.org/10.5327/Z2317-4889201400020008.
Klein, E.L., Lopes, E.C.S., Chaves, C.L., 2015. Geologia e Recursos Minerais da Folha. Santa Luzia do Pará – SA.23-V-C-VI, Estado do Pará, Escala 1:100.000. Belém, CPRM, CD-ROM (in Portuguese).
Klein, E.L., Lopes, E.C.S., Tavares, F.M., Campos, L.D., Souza-Gaia, S.M., Neves, M.P., Perrotta, M.M., 2017. Áreas de Relevante Interesse Mineral: Cinturão Gurupi, estados do Pará e Maranhão. Informe de Recursos Minerais, Série Províncias Minerais do Brasil, 11, Brasília. CPRM – Serviço Geológico do Brasil, p. 206 (in Portuguese).
Laurent, O., Martin, H., Moyen, J.-F., Doucelance, R., 2014. The diversity and evolution of late-Archean granites: evidence for the onset of a "modern-style" plate tectonics between 3.0 and 2.5 Ga. Lithos 205, 208–235.
Lesquer, A., Beltrão, J.F., Abreu, F.A.M., 1984. Proterozoic links between northeastern Brazil and West Africa: a plate tectonic model based on gravity data. Tectonophysics 110, 9–26.
Li, W.-X., Li, X.-H., 2003. Adakitic granites within the NE Jiangxi ophiolites, South China: geochemical and Nd isotopic evidence. Precambrian Res. 12, 29–44.
Lopes, E.C.S., Klein, E.L., Moura, C.A.V., Lucas, F.R.A., Pinheiro, B.L.S., Rodrigues, J.B., Simas, M.W., 2016. U-Pb (LA-ICP-MS) of detrital zircon and whole rock Nd and geochemical constraints on the provenance, depositional age and tectonic setting of the metasedimentary Piriá Basin, northern Brazil: implications for the evolution of the Gurupi Belt. Braz. J. Genet. 46, 123–144.
Lowell, G.R., Villas, R.N.N., 1983. Petrology of nepheline syenite gneiss from Amazonian Brazil. Geol. J. 18, 53–75.

Ludwig, K.R., 2003. User's Manual for Isoplot/Ex Version 3.00 – A Geochronology Toolkit for Microsoft Excel, vol. 4. Berkeley Geochronological Center Special Publication, No, p. 70pp.

Machado, N., Gauthier, G., 1996. Determination of $^{207}Pb/^{206}Pb$ ages on zircon and monazite by laser ablation ICPMS and application to a study of sedimentary provenance and metamorphism in southeastern Brasil. Geochem. Cosmochim. Acta 60 (24), 5063–5073.

McFarlane, H.B., Ailleres, L., Betts, P., Ganne, J., Baratoux, L., Jessell, M.W., Block, S., 2019. Episodic collisional orogenesis and lower crust exhumation during the Palaeoproterozoic Eburnean Orogeny: evidence from the Sefwi greenstone belt, West African craton. Precambrian Res. 325, 88–110.

Meredith, A.S., Collins, A.S., Williams, S.E., Pisarevsky, S., Foden, J.D., Archibald, D.B., Blades, M.L., Alessio, B.L., Armistead, S., Plavsa, D., Clark, C., Müller, R.D., 2017. A full-plate global reconstruction of the Neoproterozoic. Gondwana Res. 50, 84–134.

Moreira, H., Seixas, L., Storey, C., Fowler, M., Lasalle, S., Stevenson, R., Lana, C., 2018. Evolution of Siderian juvenile crust to Rhyacian high Ba-Sr magmatism in the Mineiro belt, southern São Francisco craton. Geosci. Front. 9, 977–995.

Nance, R.D., Murphy, J.B., Santosh, M., 2014. The supercontinent cycle: a retrospective essay. Gondwana Res. 25, 4–19.

Nelson, B.K., DePaolo, D.J., 1985. Rapid production of continental crust 1.7 to 1.9 b.y. ago: Nd isotopic evidence from the basement of the North American mid-continent. Geol. Soc. Am. Bull. 96, 746–754.

Nogueira, B.K.C., Gorayeb, P.S.S., Dantas, E.L., Leal, R.E., Galarza, M.A., 2017. Rhyacian evolution of the eastern São Luís Craton: petrography, geochemistry and geochronology of the Rosário Suite. Braz. J. Genet. 47, 275–299. https://doi.org/10.1590/2317-4889201720160114.

Nunes, K.C., 1993. Interpretação integrada da Bacia do Parnaíba com ênfase nos dados aeromagnéticos. In: Congresso Internacional da Sociedade Brasileira de Geofísica, 2, vol. 1. Resumos Expandidos, pp. 152–157 (in Portuguese).

Oliveira, R.G., 2016. Interpretação dos dados gravimétricos do Cinturão Gurupi. CPRM (Unpublished internal report).

Oriolo, S., Oyhantçabal, P., Wemmer, K., Siegesmund, S., 2017. Contemporaneous assembly of Western Gondwana and final Rodinia break-up: implications for the supercontinent cycle. Geosci. Front. 8, 1431–1445.

Paces, J.B., Miller, J.D., 1993. Precise U-Pb ages of Duluth Complex and related mafic intrusions, Northeastern Minnesota: geochronological insights to physical, petrogenic, paleomagnetic and tectonomagmatic processes associated with the 1.1 Ga midcontinent rift system. J. Geophys. Res. 98B, 13997–14013.

Palheta, E.S., Abreu, F.A.M., Moura, C.A.V., 2009. Granitóides proterozóicos como marcadores da evolução geotectônica da região nordeste do Pará. Brasil. Revista Brasileira de Geociências 39, 647–657 (in Portuguese).

Pastana, J.M.N., 1995. Programa Levantamentos Geológicos Básicos do Brasil. Programa Grande Carajás. Turiaçu/Pinheiro, folhas SA.23-V-D/SA.23-Y-B. Estados do Pará e Maranhão. Brasília. Companhia de Pesquisa de Recursos Minerais, 205pp (in Portuguese).

Peng, T.P., Wilde, S.A., Fan, W.M., Peng, B.X., 2013. Late Neoarchean potassic high Ba–Sr granites in the Taishan granite–greenstone terrane: petrogenesis and implications for continental crustal evolution. Chem. Geol. 344, 23–41.

Pearce, J.A., 1982. Trace element characteristics of lavas from destructive plate boundaries. In: Thorpe, R.S. (Ed.), Andesites: Orogenic Andesites and Related Rocks. Wiley, Chichester, p. 525.

Pearce, J.A., 1996. A user's guide to basalt discrimination diagrams. In: Wyman, D.A. (Ed.), Trace Element Geochemistry of Volcanic Rocks: Applications for Massive Sulfide Exploration, vol. 12. Geological Association of Canada, Short Course Notes, pp. 79–113.

Pearce, J.A., 2008. Geochemical fingerprinting of oceanic basalts with applications to ophiolite classification and the search for Archean oceanic crust. Lithos 100, 14–48.

Pearce, J.A., Harris, N.B.W., Tindle, A.G., 1984. Trace element discrimination diagrams for the tectonic interpretation of granitic rocks. J. Petrol. 25, 956–983.

Petersson, A., Scherstén, A., Andersson, J., Möller, C., 2013. Zircon U–Pb and Hf–isotopes from the eastern part of the Sveconorwegian Orogen, SW Sweden: implications for the growth of Fennoscandia. In: Roberts, N.M.W., Van Kranendonk, M., Parman, S., Shirey, S., Clift, P.D. (Eds.), Continent Formation through Time, vol. 389. Geological Society, London, Special Publications. https://doi.org/10.1144/SP389.2.

Pinheiro, B.L.S., Moura, C.A.V., Klein, E.L., 2003. Estudo de proveniência em arenitos das formações Igarapé de Areia e Viseu, nordeste do Pará, com base em datação de monocristais de zircão por evaporação de chumbo. In: 8th Simpósio de Geologia da Amazônia, Resumos Expandidos (CD-ROM) (in Portuguese).

Pisarevsky, S., Elming, S.A., Pesonen, L.J., Li, Z.X., 2014. Mesoproterozoic paleogeography: supercontinent and beyond. Precambrian Res. 244, 207–225.

Polat, A., Hofmann, A.W., Rosing, M.T., 2002. Boninite-like volcanic rocks in the 3.7–3.8 Ga Isua greenstone belt, West Greenland: geochemical evidence for intra-oceanic subduction zone processes in the early Earth. Chem. Geol. 184, 231–254.

Poujol, M., Kiefer, R., Robb, L.J., Anhaeusser, C.R., Armstrong, R.A., 2005. New U–Pb data on zircons from the Amalia greenstone belt, southern Africa: insights into the Neoarchaean evolution of the Kaapvaal craton. S. Afr. J. Geol. 108, 317–332.

Ribeiro, J.W.A., 2002. O arcabouço estrutural da região de Chega Tudo e Cedral, NW do Maranhão, com base em sensores geofísicos. M.Sc. Thesis. Universidade Federal do Pará, Belém, Brazil, p. 155 (in Portuguese).

Richards, J.P., Kerrich, R., 2007. Special paper: adakite-like rocks: their diverse origins and questionable role in metallogenesis. Econ. Geol. 102, 537–576.

Rosa, M.L.S., Conceição, H., Macambira, M.J.B., Marinho, M.M., Marques, L.S., 2003. Idade (Pb-Pb) e aspectos petrográficos e litogeoquímicos do Complexo Alcalino Floresta Azul, sul do estado da Bahia. Rev. Bras. Geociencias 33 (1), 13–20 (in Portuguese).

Rudnick, R.L., Gao, S., 2005. Composition of the continental crust. In: Rudnick, R.L. (Ed.), The Crust, Treatise on Geochemistry, vol. 3. Elsevier-Pergamon, Oxford, pp. 1–64.

Santos, J.O.S., Hartmann, L.A., Bossi, J., Campal, N., Schipilov, A., Piñeyro, D., McNaughton, N.J., 2003. Duration of the trans-amazonian cycle and its correlation within south America based on U–Pb SHRIMP geochronology of the La plata craton, Uruguay. Int. Geol. Rev. 45, 27–48.

Sato, K., Siga Jr., O, 2000. Evidence of the superproduction of the continental crust during Paleoproterozoic in South American Platform. Implications regarding the interpretative value of the Sm/Nd model ages. Rev. Bras. Geociencias 30, 126–129.

Schmitt, R.S., Fragoso, R.A., Collins, A.S., 2018. Suturing Gondwana in the Cambrian: The Orogenic Events of the Final Amalgamation. In: Siegesmund, S., Basei, M., Oyhantçabal, P., Oriolo, S. (Eds.), Geology of Southwest Gondwana. Regional Geology Reviews. Springer, Cham, pp. 411–432.

Sheppard, S., Bodorkos, S., Johnson, S.P., Wingate, M.T.D., Kirkland, C.L., 2010. The Paleoproterozoic Capricorn Orogeny: intracontinental reworking not continent–continent collision. Geol. Surv. West. Aust., Rep. 108, 33p.

Spencer, C.J., Kirkland, C.L., Taylor, R.J.M., 2016. Strategies towards statistically robust interpretations of in situ U-Pb zircon geochronology. Geosci. Front. 7, 581–589.

Stacey, J.S., Kramers, J.D., 1975. Approximation of terrestrial lead isotope evolution by a 2-stage model. Earth Planet Sci. Lett. 26 (2), 207–221.

Streckeisen, A.L., 1976. To each plutonic rock its proper name. Earth Sci. Rev. 12, 1–33.

Sun, S.S., McDonough, W.F., 1989. Chemical and isotopic systematics of oceanic basalts: implications for mantle compositions and processes. In: Saunders, A.D., Norry, M.J. (Eds.), Magmatism in Ocean Basins, vol. 42. Geological Society, London Special Publications, pp. 313–345.

Tarney, J., Jones, C.E., 1994. Trace element geochemistry of orogenic igneous rocks and crustal growth models. J. Geol. Soc. Lon. 151, 855–868.

Tavares, F.M., Klein, E.L., Lopes, E.C.S., Souza-Gaia, S.M., Paleoproterozoic and Neoproterozoic Orogenies Superposed in the Gurupi Belt, Northern Brazil: Evidence from Structural Geology and Airborne Geophysics. (in review).

Taylor, S.R., McLennan, S.M., 1985. The Continental Crust: its Composition and Evolution. Blackwell Scientific Publications, Oxford, pp. 1–312.

Torquato, J.R., Cordani, U.G., 1981. Brazil–Africa geological links. Earth Sci. Rev. 17, 155–176.

Uyeda, S.K.H., Kanamori, H., 1979. Back-arc opening and the mode of subduction. J. Geophys. Res. 84, 1049–1061.

Villas, R.N.N., 1982. Geocronologia das intrusões ígneas na bacia do rio Guamá, nordeste do Estado do Pará. In: 2nd Simpósio de Geologia da Amazônia, Anals, vol. 1, pp. 233–247 (in Portuguese).

Villas, R.N.N., Sousa, F.D.S., 2007. O granito de duas micas Ney Peixoto, nordeste do Pará: aspectos petrológicos e significado tectônico. Rev. Bras. Geociencias 37, 3–16 (in Portuguese).

Villeneuve, M., 2008. In: Enni, N., Liégeois, J.P. (Eds.), Review of the Orogenic Belts on the Western Side of the West African Craton: the Bassarides, Rokelides and Mauritanides, vol. 297. Geological Society of London, Special Publications. https://doi.org/10.1144/SP297.8.

Whalen, J.B., Currie, K.L., Chappell, B.W., 1987. A-type granites: geochemical characteristics, discrimination and petrogenesis. Contrib. Mineral. Petrol. 95, 407–419.

Whalen, J.J.B., Pehrsson, S.J.P., Rayner, M.N., 2016. Significance of pre-1860 Ma granitoid magmatism for crustal evolution and exploration targeting in the Flin Flon assemblage, Trans-Hudson Orogen, Canada. Econ. Geol. 111, 1021–1039.

Williams, I.S., 1998. U-Th-Pb geochronology by ion microprobe. In: McKibben, M.A., Shanks III, W.C., Ridley, W.I. (Eds.), Applications of Microanalytical Techniques to Understanding Mineralizing Processes. Reviews in Economic Geology, vol. 7, pp. 1–35.

Wilson, M., 1989. Igneous Petrogenesis: A Global Tectonic Approach. Chapman & Hall, London, p. 466.

Winchester, J.A., Floyd, P.A., 1977. Geochemical discrimination of different magma series and their differentiation products using immobile elements. Chem. Geol. 20, 325–343.

Winter, J.D., 2001. Introduction to Igneous and Metamorphic Petrology. Prentice Hall, New Jersey, p. 697.

Yamaguti, H.S., Villas, R.N.N., 2003. Estudo microtermométrico dos fluidos hidrotermais relacionados com a mineralização aurífera de Montes Áureos, NW do Maranhão. Rev. Bras. Geociencias 33, 21–32 (in Portuguese).